



**Facultad
de
Ciencias**

**Comparative study of the band structure of
CaTiO₃, SrTiO₃ and BaTiO₃**

(Estudio comparativo de la estructura de bandas de
CaTiO₃, SrTiO₃ y BaTiO₃)

Trabajo de Fin de Grado
para acceder al

GRADO EN FÍSICA

Autor: Patricia Fernández de Cos

Director: Francisco Javier Junquera Quintana

Diciembre - 2019

Agradecimientos

En primer lugar, me gustaría agradecer a todos los docentes que me han guiado en el camino hacia la finalización de este trabajo: a Carmen, por moldear este cerebro en sus inicios; a Teresa, por introducirme en el mundo de la física; a Gema, por dejarme entrever el horror de las matemáticas; a Santiago, por hacer brotar en mí una actitud crítica; a Ana, por transmitirme el gusto por los idiomas y, por último, a Javier Junquera, por haberme permitido realizar este trabajo.

En segundo lugar, quisiera ensalzar el papel de Alexandra Elbakyan, creadora de Sci-Hub; gracias por promover una visión de ciencia abierta tan necesaria para permitir el desarrollo de la sociedad moderna.

Asimismo, me gustaría dar también las gracias a las personas que han estado a mi lado durante esta aventura que hoy llega a su fin: a mi familia, por haberme apoyado en mis días malos y, sobre todo, por no haber puesto jamás ninguna barrera ni en mi formación educativa ni en mi desarrollo personal; a mis amigos, por ser una fuente de alegría e inspiración continua y, finalmente, a mis compañeros de clase. En especial, me gustaría dar las gracias de corazón a Fran, a Pablo, a Mónica, a Raquel, a Diego, a Masterclass y a mis matemáticos favoritos; sois, sin lugar a duda, lo que me llevo de esta etapa.

Por último, quisiera dar las gracias a una persona muy importante para mí que no es otra sino yo. Gracias a mi yo más pesimista por haber cedido ante la presión de mi yo más luchador y haber llegado, otra vez más, a la meta.

Abstract

Perovskite-like structures and, in particular, perovskite-like oxides (ABO_3) have been deeply studied since the discovery of $CaTiO_3$ in 1839 due to their wide range of physical properties and potential industrial uses (e.g non-volatile computer memories, IR sensors, etc).

This bachelor thesis has been focused on the characterisation of both the high-symmetry and low-symmetry phases of $CaTiO_3$, $SrTiO_3$ and $BaTiO_3$, which are embedded in the so-called II-IV perovskite family, by means of first-principles simulations performed in the framework of DFT. Even though the only difference between them lies in the A cation, it is well known that the type of instability displayed by each perovskite-like structure in its low-temperature phases is significantly different: the ground state of $CaTiO_3$ and $SrTiO_3$ exhibits TiO_6 octahedral rotations (i.e an AFD instability) whereas the one of $BaTiO_3$, as well as its low-temperature tetragonal phase, displays a non-null macroscopic polarization (i.e an FE instability).

In order to characterise the high-symmetry phase (i.e the bulk cubic structure) of the aforesaid perovskite-like oxides, the band structure, the Projected Density of States, the so-called “fat bands”, the Born effective charge tensor and the bond lengths of these crystalline structures have been computed and carefully analysed. As a result of such analysis, the following main conclusions have been drawn: the bottom of the conduction band has a predominant $Ti-t_{2g}$ character whereas the top of the valence band is mainly composed of $O-2p$ orbitals and the bonds arising between these orbitals display a mixed covalent-ionic nature.

In addition, the structural properties of the low-symmetry phases of the aforementioned perovskites (i.e of the ground state of $CaTiO_3$ and $SrTiO_3$ and of the tetragonal phase of $BaTiO_3$) have been also studied with the ultimate goal of analysing their different nature which is a manifestation of the predominant soft mode arising in that crystalline structure. The results obtained regarding the unit cell characterisation (e.g lattice parameters, atomic positions, rotation angles, etc.) have been found to be in full agreement not only with the type of instabilities predicted by means of the Goldschmidt Tolerance Factor but also with the structural parameters obtained through either neutron or X-ray diffraction. Moreover, the macroscopic polarization displayed by the tetragonal phase of $BaTiO_3$ has been computed yielding the numerical value $P_z = 30.39\mu C \times cm^{-2}$.

Key words: Perovskites, first-principles simulation, AFD, FE, Goldschmidt Tolerance Factor.

Resumen

Las estructuras de tipo perovskita y, en concreto, los óxidos de tipo perovskita (ABO_3) han sido ampliamente estudiados desde el descubrimiento del $CaTiO_3$ en 1839 debido a su amplio rango de propiedades físicas y a sus potenciales usos industriales (por ejemplo, memorias de ordenadores no volátiles, sensores IR, etc).

Este TFG se ha centrado en la caracterización tanto de las fases de alta simetría como de las fases de baja simetría del $CaTiO_3$, del $SrTiO_3$ y del $BaTiO_3$, que pertenecen todos ellos a la llamada familia de perovskitas II-IV, mediante simulaciones de primeros principios en el marco de la teoría DFT. A pesar de que la única diferencia entre ellos reside en el catión A, es bien sabido que el tipo de inestabilidad exhibida por cada una de las ya mencionadas estructuras de tipo perovskita en sus fases de baja temperatura es considerablemente distinto: el estado fundamental del $CaTiO_3$ y del $SrTiO_3$ exhibe rotaciones de los octaedros TiO_6 (es decir, una inestabilidad AFD) mientras que el del $BaTiO_3$, así como su fase tetragonal de baja simetría, se caracteriza por un valor no nulo de la polarización macroscópica (es decir, una inestabilidad FE).

Con el objetivo de caracterizar la fase de alta simetría (es decir, la estructura cúbica) de los óxidos de tipo perovskita mencionados con anterioridad, la estructura de bandas, la Densidad Proyectada de Estados, las llamadas “bandas gordas”, el tensor de carga efectiva de Born y las longitudes de enlace de estas estructuras cristalinas han sido calculados y analizados cuidadosamente. Como consecuencia de dicho análisis, las siguientes conclusiones principales han sido obtenidas: la parte inferior de la banda de conducción tiene un carácter $Ti-t_{2g}$ predominante mientras que la parte superior de la banda de valencia está compuesta principalmente por orbitales $O-2p$ y los enlaces que tienen lugar entre dichos orbitales exhiben una naturaleza mixta entre enlaces iónicos y covalentes.

Además, las propiedades estructurales de las fases de baja simetría de las perovskitas mencionadas con anterioridad (es decir, del estado fundamental del $CaTiO_3$ y del $SrTiO_3$ y de la fase tetragonal del $BaTiO_3$) han sido estudiadas también con el fin último de analizar su diferente carácter que es una manifestación del modo suave que surge en estas estructuras cristalinas. Los resultados obtenidos con respecto a la caracterización de la celda unidad (por ejemplo, los parámetros de red, las posiciones atómicas, los ángulos de rotación, etc.) han demostrado estar en perfecta consonancia no solo con el tipo de inestabilidades predichas por el Factor de Tolerancia de Goldschmidt sino también con los parámetros estructurales obtenidos a través de bien difracción de neutrones, bien difracción de rayos X. Asimismo, la polarización macroscópica exhibida por la fase tetragonal del $BaTiO_3$ ha sido calculada obteniéndose el valor numérico $P_z = 30.39\mu C \times cm^{-2}$.

Palabras clave: Perovskitas, simulación de primeros principios, AFD, FE, Factor de Tolerancia de Goldschmidt.

Contents

1	Introduction	1
1.1	ABO ₃ perovskite structure	1
1.2	Technological applications	2
1.3	Ferroelectricity and oxygen octahedral rotations	3
1.4	Soft mode approach	8
1.5	Low-Temperature stable phases	10
1.6	Objectives of this bachelor thesis	11
2	Computational Methods	12
2.1	Implemented approximations	12
2.2	First-principles codes	14
3	Cubic phase characterisation of CaTiO₃, SrTiO₃ and BaTiO₃	17
3.1	Lattice constant	17
3.2	Coordination number and bond lengths	18
3.3	Band structure	18
3.4	Born effective charges	21
3.5	Maximally Localized Wannier Functions	22
4	Ground state characterisation of CaTiO₃, SrTiO₃ and BaTiO₃	26
4.1	Geometrical Optimization	26
4.2	Structural Properties	27
5	Final considerations	37
5.1	Conclusions	37
5.2	Future work	38
	Appendices	40
	Appendix A: Further physical concepts	40

Chapter 1

Introduction

The aim of this chapter is to characterise the unlike low-temperature stable phases of the three perovskite-like titanates (CaTiO_3 , SrTiO_3 and BaTiO_3) that will be analysed throughout this work as well as to explain the origin of both the ferroelectricity and the octahedral rotations displayed by some of them.

1.1 ABO_3 perovskite structure

ABO_3 type oxides, such as the ones mentioned above, are of great importance nowadays due to the fact that they display a wide range of physical properties including ferroelectricity, piezoelectricity and ferromagnetism, among others, that can be controlled by their electronic configuration, their ion size, etc, which enables the possibility of tuning one of these properties via material engineering.

The ideal perovskite structure, which is often distorted leading to other phases accounting for an upgraded energetic stability, such as the orthorhombic and tetragonal ones that will be explained later on, presents a cubic unit cell and can be classified within the $\text{Pm}\bar{3}\text{m}$ space group. As it can be seen in Figure 1.1, if one chooses the unit cell so as to have the B ion located at its body centre, the atomic positions of A, B and O-like atoms are given by $[0,0,0]$, $[1/2, 1/2, 1/2]$, $[1/2, 1/2, 0]$, $[1/2, 0, 1/2]$ and $[0, 1/2, 1/2]$ respectively. Besides, if one quickly inspects the same figure, it is straightforward to realize that A-like atoms have a 12-fold oxygen coordination whilst each B-like atom is only surrounded by 6 oxygens which are, each, linked to six cations ($4\text{A} + 2\text{B}$).

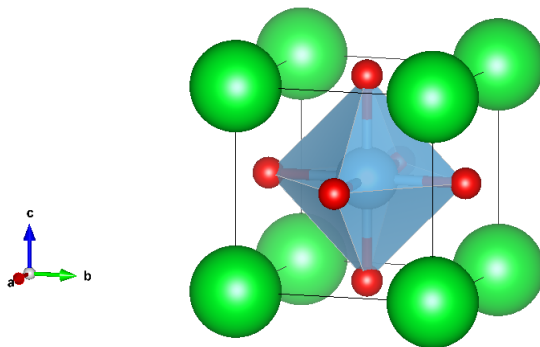


Figure 1.1: Schematic view of an ABO_3 ideal cubic structure where the A and B ions are represented by green and blue spheres, respectively, whereas the oxygens are represented by red ones. Image obtained using VESTA [1].

It is worth remarking that the same crystalline structure can be alternatively depicted as a three dimensional A-centred cubic network consisting of eight rigid corner-sharing BO_6 octahedra.

1.2 Technological applications

If one inspects the theoretical background concerning the aforementioned perovskite-like structures it is straightforward to realise that these materials have been deeply analysed over the last fifty years due to the wide range of properties exhibited by them and, therefore, to their potential use in several industries.

As a result of their intrinsic properties arising from their atomic constituents and the arrangement of the former within the crystalline structure, perovskite-like oxides, in which CaTiO_3 , SrTiO_3 and BaTiO_3 are embedded, have proven not only to work efficiently as catalysts because of their high melting point but also to constitute successful oxygen flow carriers owing to their elevated densities [2] [3].

In spite of the importance of these properties regarding the chemical market, ferroelectricity, which, as it will be later explained, is only exhibited by those perovskite-like structures displaying a polar arrangement (i.e for a non centre-symmetric structure), has been the most exploited feature to date. Among the numerous technological applications linked to ferroelectric perovskite-like oxides, the use of these materials as electro-optic switching devices all along with their utility regarding the manufacturing process of non-volatile computer memories, constitute the most remarkable ones. However, for the shake of brevity, only the second application will be briefly explained in this present work.

Bearing in mind that the essential prerequisite for manufacturing a computer memory, either a ROM or a RWM, is that there must be two distinct physical states of the core components that can be assigned to a logical 1 or 0, it is therefore natural to consider bulk ferroelectric materials as perfect candidates regarding the manufacturing process as both logical states could be identified with each remanent polarization state. Furthermore, the use of ferroelectric materials as core components of computer memories exhibits a clear advantage in terms of information retrieval: because of the hysteresis loop presented among these type of materials, no information will be lost in the case of a power shutdown.

In order to manufacture a non-volatile computer memory exhibiting a high performance as well as a decent data storage capacity, it is mandatory to assemble as many devices as desired bits into an array of, usually, silicon-based electrodes. It is then clear that bulk materials can no longer be used and, with the aim of overcoming this issue, thin nanometric perovskite-like oxide layers are used in their place. By doing so not only the memory is improved in terms of size but also in terms of commutation speed as it can be proved that a reduction of the size of the aforementioned layer leads to a decrease in the numerical value of the coercive field too (i.e the magnitude of the electric field needed to switch the polarization) as long as the offset of ferroelectricity is not attained [4].

1.3 Ferroelectricity and oxygen octahedral rotations

In this present section the two main unstable modes of the already explained perovskite structure (i.e oxygen octahedral rotations, hereinafter referred to as AFD, and ferroelectricity, hereinafter referred to as FE) will be explained. Moreover, an empirical rule for predicting structural distortions based on steric arguments will be analysed and, finally, a brief analysis of the competition and cooperative couplings between AFD and FE will be made.

1.3.1 Oxygen octahedral rotations

1.3.1.1 General overview

The structures displaying oxygen octahedral rotations, which are very stable in wide ranges of temperature and pressure, transform into different crystal systems (e.g tetragonal or orthorhombic) that are, indeed, more present among ABO_3 perovskites than the cubic one.

According to Glazer [5], there are 23 distinct systems regarding octahedral tilting which are, each, classified in terms of three letters (a,b and c), each of them indicating the magnitude of the tilt along the direction of the axes [100], [010] and [001] respectively; as well as in terms of three symbols (+, - and 0), each of them denoting an in-phase tilting between successive oxygen octahedra defined along the same axis, an anti-phase tilting or no tilting at all respectively. It is worth noting that the presence of in-phase rotation patterns does not exclude the presence of anti-phase ones along different axes although they tend to cancel each other out as it was reported in [6] for the $a^-a^-c^+$ ground state displayed by roughly half of the perovskite oxydes.

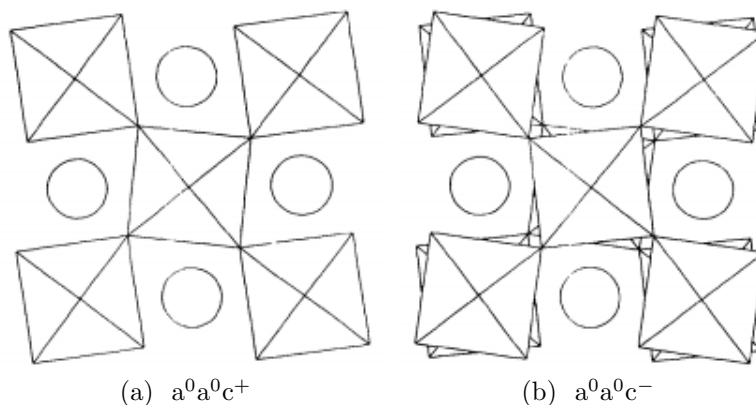


Figure 1.2: Schematic view looking down the c axis of a two layered perovskite structure displaying either an in-phase rotation pattern along the c axis, Figure 1.2a, or an anti-phase rotation pattern along the same axis, Figure 1.2b. Image taken from [7].

As it can be seen in Figure 1.2, oxygen octahedral rotation patterns mainly consist in rigid rotations of the BO_6 octahedra that, even though they do not modify the coordination sphere of the B ion which is embedded in the central part of it, they do significantly change the one relative to the A cation.

1.3.1.2 Bonding approach

Chemical bonding [8] plays an important role when inferring which of the 23 Glazer's systems will be displayed by a given perovskite as a result of an instability that can be usually predicted by means of the Goldschmidt Tolerance Factor which will be explained later on. In order to understand such phenomenon, both ionic and covalent bonding have been deeply analysed in the last decade, paying important attention to the latter which can be split into A/B-O σ and B-O π bonding, being this one only significant in the case of having a transition metal acting as the B atom which is, indeed, the case that will be treated throughout this work.

It is beyond the scope of this work to explain the mathematical models that have been used to study the relationship between chemical bonding and rotation amplitude and "sense" (i.e in-phase or anti-phase rotation patterns) among ABO_3 perovskites, which are, mainly, that related to a local pseudo Jahn-Teller effect [9], a covalency metric [10] and a group theoretical analysis based on the irreps of the $Pm\bar{3}m$ space group [11]. However, for the sake of completeness, the most significant conclusions yielded by these analysis will be stated below:

- **A-O bonding:** Because of the large difference regarding electronegativity between typical A cations and O atoms, this type of bonding is expected to be highly ionic [12]. However, as the electronegativity of the former increases, the importance of the covalent bonding between these two species will increase too, being specially significant as the distortion from the ideal cubic structure, also referred to as $a^0a^0a^0$ using Glazer's notation, increases, due to the augmented overlap of oxygen orbitals with the A cation [12]. Finally, the $a^+b^-b^-$ Glazer system, which is embedded in the $Pnma$ space group and, thus, displays an orthorhombic crystal structure, has been found to be the one that maximizes A-O covalent bonding and, at the same time, minimizes their repulsive overlap. It is because of that fact that such Glazer system can be largely found for structures accounting for a small Tolerance Factor and a highly electronegative A cation.
- **B-O bonding:** Even though a competition for the same orbitals within the oxygen has been reported between the σ bonding orbitals of the A cation and the π ones of the B counterpart [12], the interactions of the latter cation with the oxygen are expected to be stronger than the ones arising from the interaction of the former ion as, this one, is usually less electronegative. It is worth remarking that, since AFD does not change the coordination sphere of the B cation, as it was explained above, and, besides, the distances between the B cation and the O anion barely change, the analysis of this type of bonding lies in the modification of the B-O-B angles which, in the cubic structure, are reported to be 180° [12]. Finally, the $a^0a^0a^0$ Glazer system has been found to be the one that maximizes B-O covalent bonding being, in fact, only observed for structures accounting for oversized A cations and significant B-O π bonding.
- **$a^0a^0a^0$ stability:** Even though B-O covalent bonding is greatly maximized when a cubic structure is displayed by a given perovskite, it is known, and it has been already stated in this present work, that most perovskites do not possess the ideal cubic $Pm\bar{3}m$ symmetry (i.e the $a^0a^0a^0$ Glazer system) but undergo symmetry-lowering distortions. In terms of bonding this can be understood by the fact that, for small tilting angles, the increase in ionic energy associated with the aforementioned

$a^+b^-b^-$ Glazer system largely outweighs the B-O covalent bonding stabilization of the former structure [12].

Keeping in mind that the energy, spatial extent and filling of the different orbitals within the chemical species of a given perovskite oxide will play a crucial role in terms of bonding strength, it is necessary to analyse the evolution of its Density of States, hereinafter referred to as DOS, and/or its Projected Density of States, hereinafter referred to as PDOS, so as to check which atoms significantly contribute to it below the Fermi level (see [13] for further information concerning DOS and PDOS).

1.3.2 Ferroelectricity

1.3.2.1 General overview

Bulk ferroelectricity, which can only be understood in terms of a collective model as it will be explained in the following section, was first discovered in 1920 through the study of Rochelle salt [14] and has been deeply studied since due to its technological applications such as dielectric capacitors or IR sensors among others (see [15] for further information regarding bulk ferroelectricity technological applications).

Multiple approaches are still being currently used in order to analyse the global mechanism responsible for ferroelectric transitions such as hybridization between the formally empty d states of the transition metal B and the oxygen- $2p$ states, which is modelled as a second-order Jahn Teller effect [16], lattice dynamics concerning the so-called soft mode (see Section 1.4) [17] and Born effective charges [18] among others. However, all of them ultimately agree in the fact that ferroelectricity must be considered as a cooperative phenomenon in such a way that its appearance in one part of the structure leads to an electrostatic field which results in a similar polarisation in neighbouring parts.

For a material to be considered ferroelectric, being ferroelectricity linked to pyroelectricity and piezoelectricity, it must possess at least two equilibrium orientations of the spontaneous polarization vector in the absence of an external electric field and these orientations must be possible to switch (i.e the polarization vector can be tuned) by means of a sufficiently large electric field [19].

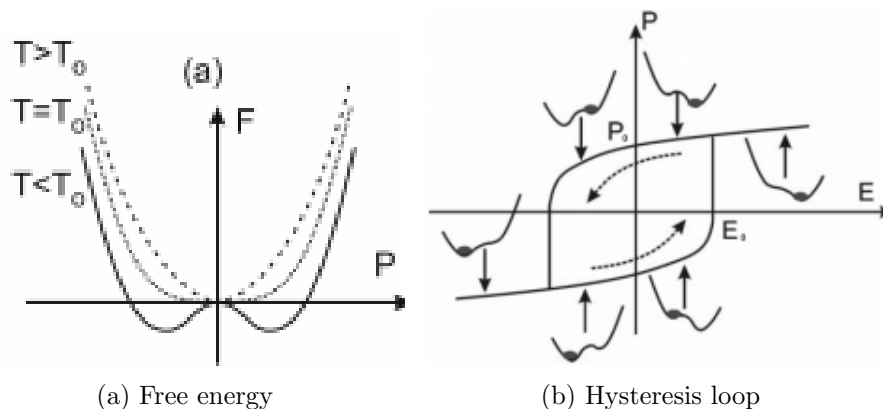


Figure 1.3: Double well-shape free energy in terms of the electric polarization, where $T_0 = T_c$, Figure 1.3a, and hysteresis loop, where P_0 and E_0 denote the remanent polarization and coercive field respectively, of a typical ferroelectric bulk material, Figure 1.3b. Image taken from [21].

Most ferroelectric bulk materials display ferroelectricity only below a certain phase transition temperature known as Curie Temperature, T_c . If one analyses that second-order phase transition by means of the Landau-Devonshire Model [20], which mainly consist in expressing the free energy of the system in terms of a contribution arising from polarization and a contribution having its origin in the strain tensor elements, the widely known hysteresis loop presented among these materials naturally arises as a certain amount of energy is required in order to overcome the barrier created by the potential surface, which adopts a double-well shape, so as to change the polarization state.

1.3.3 Classification

Multiple criteria can be followed so as to set a classification of bulk materials regarding the type of ferroelectricity that they display. Nevertheless, for the sake of brevity, just the distinction between paradigmatic ferroelectrics and incipient ferroelectrics, also referred to as quantum paraelectrics, will be analysed herein.

Paradigmatic ferroelectrics and quantum paraelectrics

Some materials such as SrTiO_3 , as it will be deeply discussed in the fourth chapter, present a polar soft mode but do not display a ferroelectricity-driven phase transition [22]. This fact, indeed, can only be understood by means of quantum paraelectricity if one wishes to remain within the soft mode framework.

In contrast to paradigmatic ferroelectricity, where ω_T reaches zero for the TO, quantum paraelectricity suppresses the onset of the ferroelectric phase transition as ω_T never reaches zero due to the stabilization of the transverse optical mode driven by quantum fluctuations [23].

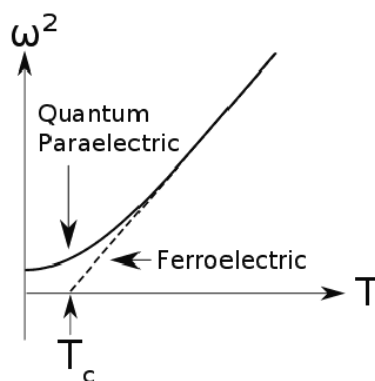


Figure 1.4: Difference regarding the TO's vibration frequency behaviour between a paradigmatic ferroelectric bulk material and a quantum paraelectric one .

1.3.4 Goldschmidt Tolerance Factor

Special importance regarding the probability of any structural distortion to be displayed is attributed to the Goldschmidt Tolerance Factor, t , [24] which quantifies that likelihood in terms of the size of each ion (A, B and O) and can be computed as it follows (see Appendix A for its step by step derivation):

$$t = \frac{R_A + R_O}{\sqrt{2}(R_B + R_O)}, \quad (1.1)$$

where R_i denotes the ionic radius of the ion I.

System	t
CaTiO ₃	0.973
SrTiO ₃	1.009
BaTiO ₃	1.070

Table 1.1: Goldschmidt Tolerance Factor of CaTiO₃, SrTiO₃ and BaTiO₃ calculated substituting the ionic radii stated by Shannon [25] in Eq.(1.1).

Theoretically speaking, it can be shown [24] that any atomic arrangement yielding a value of $t \neq 1$ (i.e not displaying an ideal cubic perovskite structure) will result in a structural distortion driven by the need to improve the bonding properties of the chemical species of the given perovskite-like structure.

In particular, the casuistry has been found to be the following:

- $t > 1$: Those perovskite-like structures yielding a numerical value of the Goldschmidt Tolerance Factor slightly greater than unity encompass an undersized B cation and, therefore, will be submitted to B-O motions which will ultimately lead to the rupture of the centrosymmetric parent phase thus resulting in a low-symmetry polar phase.
- $t < 1$: Those perovskite-like structures yielding a numerical value of the Goldschmidt Tolerance Factor slightly less than unity encompass an undersized A cation and, therefore, will be submitted to A-O motions. Specifically, such crystalline structures will display an AFD distortion which will ultimately result in a phase transition from the $a^0a^0a^0$ Glazer system to any of the 22 remaining tilted ones.

At this point it is worth mentioning that it has also been shown in [6] that, as one would expect, the energy difference between the cubic structure and the ground state varies strongly with t and so do the distortion amplitudes too being the in-phase rotation configurations and the anti-phase ones related to t in a quite similar way.

1.3.5 AFD vs FE

Even though the competition between AFD and FE modes has been largely reported among several perovskite-like structures [26] [27], recent studies have found a cooperative nature between these two instabilities giving rise to the so-called hybrid improper ferroelectricity which has ultimately set the path for electric-field control of octahedral rotations and electronic properties [28].

Although it has been proved by means of group theoretical analysis that octahedral rotations, due to its three-dimensional connectivity, can not, by themselves, induce ferroelectricity [11]; it has been found that the layering of non-polar perovskites (e.g SrTiO₃/PbTiO₃)

leads to a new type of ferroelectricity, hereinafter referred to as improper ferroelectricity due to the fact that no Γ polar instability is found, in which octahedral rotations induce an electrical polarization [29]. This phenomenon mathematically arises from the fact that a trilinear coupling of a polar mode with the octahedral rotation patterns, coming from unlike irreps (i.e the two layers display a distinct AFD mode and, therefore, they are not geometrically equivalent), is found when computing the free energy of the layered system.

Furthermore, cooperative couplings between these two modes have also been found through *ab-initio* simulations in regular LiNbO₃-type perovskites [30] which can be theoretically explained by means of a Landau-like potential expanded up to the sixth order for FE and up to the fourth for AFD. It is worth remarking that the cooperation between these two instabilities, which is believed to have a steric origin, has been found to be independent of strain and highly dependent on the amplitude of the octahedral tilting, being reinforced for great amplitudes and turning into a competitive nature for small ones [30].

1.4 Soft mode approach

This approach to understanding and anticipating unstable atomic motions, first proposed by Cochran [17], is based on the assumption that perovskites get unstable against a set of normal modes of vibration of the lattice [13] which may arise anywhere in the Brillouin zone. As a result of such instability, which can be visualized by the computation of the phonon dispersion curves that will display a negative curvature (i.e a purely imaginary vibration frequency ω), the most unstable soft mode undergoes a decrease in its frequency as the temperature decreases that leads to a frozen-phonon situation at T' (i.e the mode frequency vanishes at the transition point as expected for a second order transition) which ultimately results in a phase transition towards another symmetry which will increase ω .

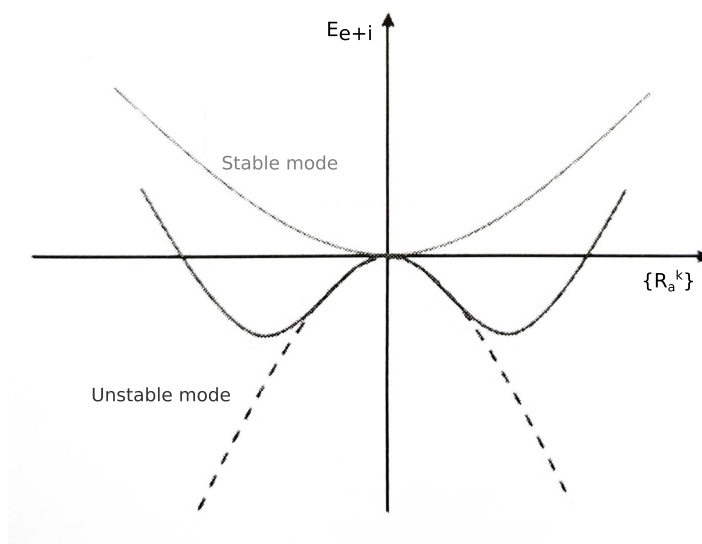


Figure 1.5: Born-Oppenheimer energy against the stable position of a nucleus belonging to an atom k within a lattice a . The upper curve displays a real vibration frequency and, therefore, represents a stable mode whereas the lower one displays an imaginary vibration frequency and, thus, represents a structure that will undergo a phase transition towards a lower energy one. The dashed curve corresponds to the harmonic oscillator solution.

An undoubtedly pitfall of this method concerning its development is the fact that one can no longer work within the harmonic oscillator framework as it has been proven [17] that anharmonicity plays a crucial role in the softening process, specially near T' , and, thus, most of the parameters of the mathematical model lying underneath the soft mode approach become linearly temperature-dependent. Furthermore, one must also take into account the dynamic non-linear coupling of the soft mode with its acoustic mode counterpart which leads to finite anomalies in the dispersion curve [31].

A clear example of the competition between the set of unstable modes can be clearly visualized in Image 1.6 where multiple normal modes of both CaTiO_3 and BaTiO_3 in their bulk cubic structure display a negative curvature.

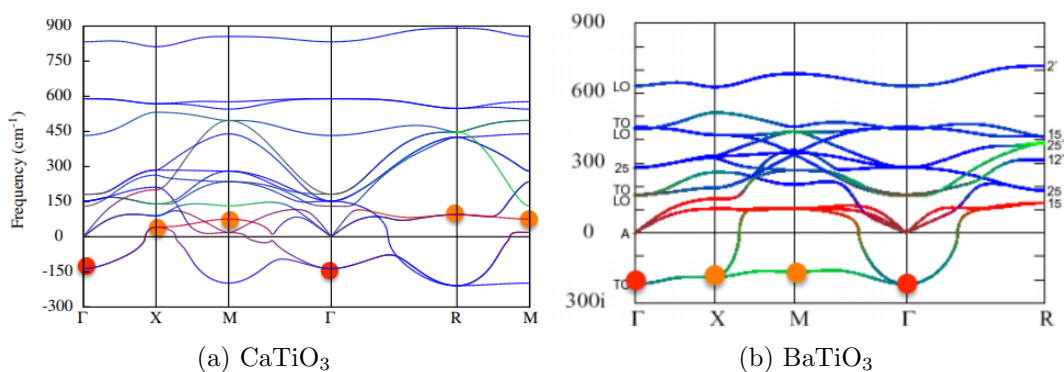


Figure 1.6: Computed phonon dispersion curves along the high symmetry lines of the Brillouin zone for both CaTiO_3 and BaTiO_3 in their bulk cubic structure. The most unstable normal modes have been identified by means of a filled circle. Image taken from [32].

When inspecting Figure 1.6 it is straightforward to realise the complexity of such approach as linking a certain phase transition with the normal mode(s) that originated it is not a trivial task. Nonetheless, for the shake of comprehension, a few words shall be said regarding unstable modes, which are labelled by a letter (the high symmetry point of the Brillouin zone where the softening process takes place), a number (the representation of the wave-vector group under which the soft mode evolves) and either a + or a - symbol denoting an in-phase or anti-phase movement, respectively, of adjacent unit cells within the supercell defined in the real space.

- Those unstable modes coming from high energetic lattice vibrations are, by and large, responsible for the distortion of the almost rigid BO_6 octahedra.
- Those unstable transverse optical modes softening at Γ , such as the Γ_4^- reported for BaTiO_3 , are directly related to FE distortions and its curvature has been found to exhibit a high degree of dependence on the volume and Born effective charges, among others, of the material considered [19]
- In general, those unstable modes softening at R and M lead to strong AFD instabilities.

1.5 Low-Temperature stable phases

It is well known that materials displaying a crystalline structure undergo structural changes (i.e changes concerning their Bravais lattice) induced by temperature or pressure among others thermodynamic parameters. In particular, perovskite-like oxides, such as the ones that will be studied throughout this present work, are characterized by their low-symmetry phases, which are mainly driven by AFD and/or FE distortions, and tend to undergo structural changes, leading to higher symmetry atomic arrangements, upon heating.

Keeping in mind that those perovskite-like structures yielding a Goldschmidt Tolerance Factor smaller than one are likely to develop an AFD instability, one can easily infer from Table 1.1 that the low-temperature phases of CaTiO_3 will display a certain Glazer system whereas those of BaTiO_3 will be driven by an FE instability. Nevertheless, the distinction between AFD and FE becomes uncertain for SrTiO_3 as its tolerance factor lies close to unity and, as a consequence, its low-temperature phases are expected to account for an admixture of both types of distortions.

Throughout this present section the different structural phase transitions exhibited by CaTiO_3 , SrTiO_3 and BaTiO_3 will be depicted leaving aside both the experimental methods carried out in order to determine each of them; which are mainly Raman spectroscopy, X-ray analysis and neutron diffraction, as well as the theoretical tools needed to study the aforementioned phase transitions, which mainly consist of a Landau-like development of the free energy of the system.

1.5.1 CaTiO_3

CaTiO_3 , as it has been already explained, has a non polar nature and, therefore, exhibits great-amplitude rotations of the TiO_6 octahedra in each of its low-temperature phases. Specifically, upon heating, it undergoes the set of structural phase transitions sketched in Figure 1.7.



Figure 1.7: Phase transitions, each of them labelled by their Glazer system, space group and crystalline structure, reported by [33] for CaTiO_3 .

1.5.2 SrTiO_3

SrTiO_3 , as it has been explained above, is embedded in the category of quantum para-electrics and, therefore, does not display any ferroelectricity-driven phase transition. In particular, it displays the AFD-driven transition depicted in Figure 1.8.

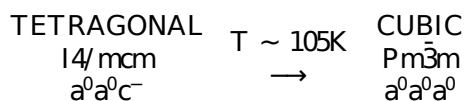


Figure 1.8: Structural phase transition labelled by its Glazer system, space group and crystalline structure reported by [34] for SrTiO_3 .

1.5.3 BaTiO₃

BaTiO₃ is a paradigmatic ferroelectric and, as a consequence, undergoes a set of phase transitions, which are sketched in Figure 1.9, driven by FE instabilities which arise from the atomic displacement of Ti towards any of the faces of the polyhedron plotted in Figure 1.1 which is, in turn, accompanied by cooperative displacements of the oxygens located within the unit cell.

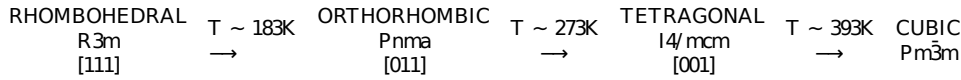


Figure 1.9: Phase transitions, each of them labelled by their spontaneous polarization axes and their space group, reported by [35] for BaTiO₃.

1.6 Objectives of this bachelor thesis

The main goal of this present bachelor thesis is to fully characterise both the high-symmetry phases (i.e the bulk cubic structure) of CaTiO₃, SrTiO₃ and BaTiO₃ as well the ground state of CaTiO₃ and SrTiO₃ (i.e the orthorhombic and tetragonal crystalline structure respectively) and the tetragonal phase of BaTiO₃ through first-principles computational simulations.

Two distinct chapters are devoted the study of the aforementioned perovskite-like oxides, which only differ from each other in the A cation and can be embedded in the so-called II-IV family:

- **Chapter 3** is intended to develop a geometrical analysis, through the computation of the lattice constant and the bond lengths; and an electronic study, through the computation of the band structure, the projected density of states and the Born effective charge tensor of the three ATiO₃ perovskite-like structures in their bulk cubic structure. The main objective of this chapter is, therefore, to explore the similarities and differences of the high-symmetry phases of these three crystals.
- **Chapter 4** is intended to investigate the FE instability of BaTiO₃ in its tetragonal structure as well as the AFD distortion that both CaTiO₃ and SrTiO₃ display in their ground state. In order to do this, all the structures will be relaxed and characterised by means of their bond lengths, projected density of states, lattice constants and, in the case of BaTiO₃, electric polarization. The main objective of this chapter is, therefore, to confirm from a first-principles simulation perspective the predictions yielded by the calculation of the Goldschmidt Tolerance Factor.

Chapter 2

Computational Methods

The aim of this chapter is to briefly review some of the approximations implemented in most of the first-principles codes currently available, including SIESTA [36], which will be the one used in order to fully characterise all the electronic and structural properties of calcium, barium and strontium titanate.

2.1 Implemented approximations

2.1.1 Born-Oppenheimer approximation

The ground state of a material composed of N_i nuclei and N_e electrons interacting among them is fully defined in terms of the time-independent Schrödinger equation as it follows:

$$H(\vec{r}, \vec{R})\Phi(\vec{r}, \vec{R}) = E\Phi(\vec{r}, \vec{R}). \quad (2.1)$$

The hamiltonian shown above is mathematically constructed as the addition of the kinetic energy operator of the nuclei and the electrons, $\hat{K}_i(\vec{R})$ and $\hat{K}_e(\vec{r})$ respectively; the nucleus-nucleus and electron-electron electrostatic interaction operators, $\hat{V}_{ii}(\vec{R})$ and $\hat{V}_{ee}(\vec{r})$ respectively; and the nucleus-electron electrostatic operator, $\hat{V}_{ie}(\vec{R}, \vec{r})$.

Keeping in mind the form of the operators, which can be consulted in [13], as well as the fact that the mass of the nuclei is way greater than that of the electrons, it can be easily shown, and its derivation is explained in very detail in [13], that, when neglecting the contribution of the kinetic energy of the nuclei (i.e when performing the Born-Oppenheimer approximation), the dynamics of the nuclei and the electrons can be decoupled and, due to their low mass, the electrons will undergo an adiabatic process in order to get adjusted to the positions of the nearly fixed nuclei.

Under the constraints mentioned above the energy of the electrons for a given nuclear arrangement characterised by an atomic structure where the nuclei occupy positions \vec{R} , $E_{el}(\vec{R})$, which is found by solving the “clamped-nuclei” Schrödinger equation, can be determined through the following expression where $K_e(\vec{r})$ represents the kinetic energy of the electrons, $E_{ee}(\vec{r})$ denotes the interaction between electrons and $E_{ie}(\vec{R}, \vec{r})$ represents the interaction energy between an electron and a nucleus:

$$E_{el}(\vec{R}, \vec{r}) = K_e(\vec{r}) + E_{ee}(\vec{r}) + E_{ie}(\vec{R}, \vec{r}). \quad (2.2)$$

2.1.2 Density Functional Theory

Even though the obtention of Eq.(2.2) might seem straightforward it is a task extremely difficult to tackle as it requires to solve an Schrödinger-like equation where the wave function depends of $4N_e$ variables ($3N_e$ spatial coordinates and $1N_e$ spin-related variable). Nowadays a wide range of methods, such as Density Functional Theory (DFT), Moller-Plesset or Hartree-Fock, have been developed in order to obtain accurate approximations for the eigenvalues of the many-body hamiltonian. Only the DFT approximation will be briefly explained in this section as it is the one that has been used throughout this work.

The key goal of DFT, which is based on the Hohenberg-Kohn Theorems (see Appendix A for further information) [37] [38], is to rewrite the energy expression shown in Eq.(2.2) as a functional of the electronic density, $n(\vec{r})$, so that the ground state energy and its electronic density can be found by minimising the electronic energy with respect to the density. This is achieved by replacing the real system of N_e interacting particles by a fictitious one of non-interacting particles yielding the same electronic charge density, mathematically constructed using Kohn-Sham orbitals (ϕ_n), which are constrained to move in an effective potential. Under these constraints E_{el} can be expressed as it follows [37]:

$$E_{el} = -\frac{1}{2} \sum_n^{N_e} \int d\vec{r} \phi_n^*(\vec{r}) \nabla^2 \phi_n(\vec{r}) d\vec{r} + \int n(\vec{r}) V_{ie}(\vec{r}) d\vec{r} + \frac{1}{2} \int \int d\vec{r} d\vec{r}' \frac{n(\vec{r}) n(\vec{r}')}{|\vec{r} - \vec{r}'|} + E_{xc}, \quad (2.3)$$

where the term E_{xc} denotes the so-called exchange-correlation energy which seeks to reflect the difference between a system of N_e interacting and non interacting particles. Multiple exchange-correlation energy functional approximations are currently available in most of the softwares performing *ab-initio* calculations. In the particular case of this work Local density Approximation, hereinafter referred to as LDA, has been implemented and, thus, the functional used throughout it adopts the following expression where ϵ_{xc}^{hom} denotes the exchange and correlation energy of an homogeneous electron gas:

$$E_{xc}^{LDA}[n(\vec{r})] = \int \epsilon_{xc}^{hom}(n(\vec{r})) n(\vec{r}) d\vec{r}. \quad (2.4)$$

2.1.3 Further approximations

Even though the above-mentioned approximations might be regarded as the principal ones it is worth mentioning the existence of others:

- **Pseudopotentials:** In order to reduce the computational effort needed to solve the many-body hamiltonian and keeping in mind that within an atom the electrons can be, usually, easily split into core electrons, which are chemically inert as its charge density remains unperturbed when adding or removing a significant number of electrons; and valence electrons, which are submitted to orthogonality constraints produced by the already mentioned core electrons, the pseudopotential approximation has been implemented throughout the calculations of this work. This approximation basically consists in replacing the effects created by the core electrons, up to a cutoff radius R_c , by an effective pseudopotential that has to be submitted to some constraints, which can be consulted in [39] and [40], regarding its norm conservation, its smoothness and its transferability.

- **Sampling of the reciprocal space:** When periodical boundary conditions are applied in a reciprocal space framework (see [13] for further information) the Bloch treatment of the eigenfunctions of the many-body hamiltonian naturally arises and, thus, those wavefunctions are unequivocally determined by a band index n and a wave vector \vec{k} . It can be shown [13] that only the wavefunctions whose $\vec{k} \in [-\frac{\pi}{a}, \frac{\pi}{a}]$ (i.e those whose \vec{k} is laying on the First Brillouin Zone, hereinafter referred to as 1BZ) produce unalike states. Keeping in mind the facts already stated above it is straightforward to realize that many physical magnitudes, such as the electronic charge density, require to compute an integral over the 1BZ. In order to reduce the computational effort a discretization is performed leading to the computation of a sum over a finite selection of k-points that will, undoubtedly, be picked regarding the smoothness of the eigenstates. Even though there are several approaches for choosing a k-grid, such as the one proposed by Chadi and Cohen [41] or that implemented by Gilat and Raubenheimer [42], the one that has been implemented in SIESTA and, thus, the one that has been used throughout this work, is the one proposed by Monkhorst and Pack (see [43] for further information).
- **Basis functions:** Keeping in mind that DFT leads to an expression of the energy functional of the real system in terms of the one-electron auxiliary functions, ϕ_n , and the electronic density, $n(\vec{r})$, it seems natural that, in order to reduce the computational cost, these mono-electronic wavefunctions should be defined as a linear combination of basis functions (whose number is significantly reduced when the pseudopotential approximation is implemented). By doing so the focus of the approach changes from the determination of the eigenstates of the Schrödinger-like equations that naturally arise in the framework of DFT to the calculation of a set of coefficients and thus, the computational effort is greatly reduced.

Multiple basis sets, which can be consulted in [44], are available in first-principles softwares. The default basis functions set by SIESTA, and the ones used throughout this work, consist of atomic orbitals which are mathematically constructed as the product of one or more different radial functions (if one wishes to improve the performance) and a spherical harmonic. Specifically, the default type is referred as DZP which stands for polarized double ζ i.e atomic basis sets that consist of two radial functions as well as polarization functions so as to improve both radial and angular flexibility (see [44] for further information).

2.2 First-principles codes

Owing to the computational development of the last decades as well as to the acquisition of knowledge regarding DFT and other related methods, which can be consulted in [45], first-principles simulations (FP), also referred to as *ab-initio*, have become extremely powerful.

FP codes are able to fully characterise a material (i.e to obtain the eigenstates of the multi-body Hamiltonian) using neither fitted parameters nor empirical models, just the fundamental physical constants. It is straightforward to see the importance of this approach as, nowadays, simulations involving a huge number of atoms are easily achievable and one can get really accurate predictions with a relatively low computational cost, specially if order-N algorithms have been implemented in the code.

2.2.1 SIESTA

Among the wide range of *ab-initio* codes currently available SIESTA [36], which was developed in the later 90s, has been the one used throughout this work. A detailed description of this code, which provides a high degree of freedom to the user and implements order-N algorithms, can be found in [46]. Nevertheless, some aspects regarding the input files and the inner algorithms used for solving the Schrödinger equation will be briefly discussed in this section.

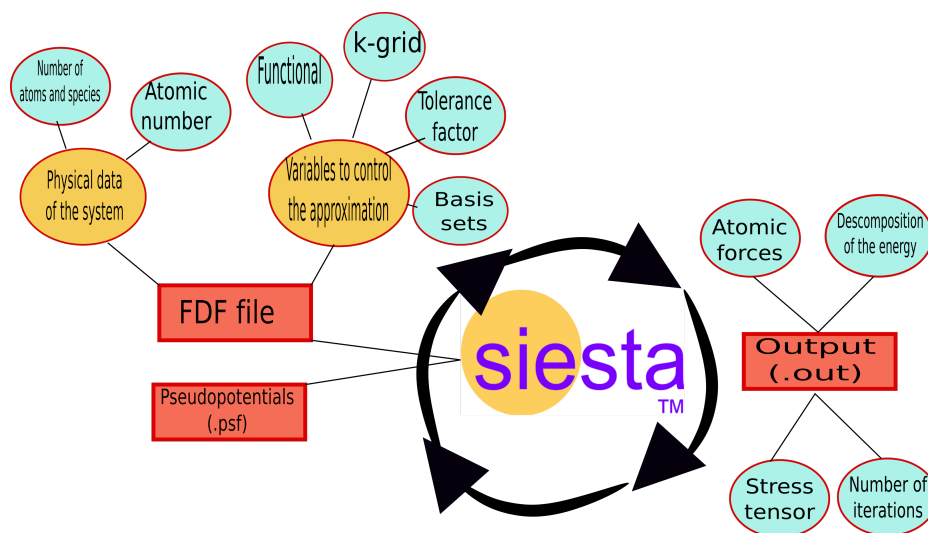


Figure 2.1: Schematic representation of the input files needed to run a simulation with SIESTA as well as the output produced after a certain number of iterations has been performed so as to solve Kohn-Sham equations self-consistently.

- **Input files:** Two different input files, as shown in Figure 2.1, are needed to perform the simulation:
 1. An input file written in Flexible Data Format (FDF) where the user has to specify the number of atoms contained in the system, the different species, the atomic number of these species, the lattice constant and vectors, etc; as well as some factors regarding the approximations already explained above such as the type of functional that will be used to perform DFT (e.g LDA, GGA, etc), the k-grid that will be used to perform the discretization within the 1BZ, the type of basis functions that will be implemented (e.g PW, Gaussians or PAO among others), the tolerance factor, etc.
 2. An input file for each kind of element defined at the ChemicalSpeciesLabel block of the FDF file, usually written in ASCII format (.psf), containing the norm conserving pseudopotential in its fully nonlocal (Kleinman-Bylander) form of the given chemical species, usually generated for their ground state.
- **Inner algorithm:** Once the hamiltonian (H) and the overlap matrices (S) have been computed with the data provided by the input files the following steps are followed in order to compute the Kohn-Sham equations self-consistently: Firstly, an initial guess for the charge densities of the isolated atoms is proposed; secondly, the effective potential is computed using the functional set in the FDF file; thirdly, the KS equation is solved and the electron density is computed and, finally, the electron density obtained is compared to the one initially proposed to see whether

the iteration has to be performed again using the first iteration density value as the initial guess or not (depending on the tolerance factor set in the FDF file).

- **Output file:** Once the previous calculation has converged an output file is produced with information regarding the different energetic terms of the system, the atomic forces and the stress tensor among others.

Chapter 3

Cubic phase characterisation of CaTiO_3 , SrTiO_3 and BaTiO_3

Even though, as it has been already pinpointed, the only perovskite-like titanate which displays a cubic structure at room temperature (i.e at 296K) is SrTiO_3 , in this present section the electronic and structural properties of the three materials will be analysed in their bulk cubic structure so as to inspect both the similarities and differences among them.

3.1 Lattice constant

In order to compute the lattice parameter of the unit cell displayed in the bulk cubic configuration of CaTiO_3 , SrTiO_3 and BaTiO_3 the total energy of each system, made up of different contributions and hereinafter referred to as E_{tot} , has been calculated for a set of i trial lattice parameters a_i , each of them defining a unit cell volume Ω_i , at a temperature of 0K. These energetic values have been later fitted to the Murnaghan equation of state [47] with the aim of obtaining the volume of the unit cell which yields the minimum energetic value and, therefore, the lattice constant for the bulk cubic structure of the three perovskite-like titanates.

System	$a_{th}/\text{\AA}$	$a_{exp}/\text{\AA}$
CaTiO_3	3.823	3.836
SrTiO_3	3.873	3.905
BaTiO_3	3.947	4.000

Table 3.1: Theoretical (th) and experimental (exp) [48] lattice parameters obtained for CaTiO_3 , SrTiO_3 and BaTiO_3 in their bulk cubic structure.

One can quickly realise that the theoretical estimation of the lattice parameter lies below the experimental one for the three perovskite-like structures. In particular, the mismatch between both values was found to be -0.34% for CaTiO_3 , -0.80% for SrTiO_3 and -1.32% for BaTiO_3 , which does not come as a surprise as the discrepancy between theoretical and experimental values concerning lattice parameter calculations within the framework of LDA was reported to lie in the range of -1% - -3% in [49].

Furthermore, the numerical values obtained, with CaTiO_3 being the perovskite-like titanate accounting for the minimum value among the three and BaTiO_3 the one displaying the biggest unit cell, are not surprisingly either as the ionic radius of Ca, Sr and Ba, which is related to the lattice parameter through the equation $a = \sqrt{2}(r_{(\text{Ca},\text{Sr},\text{Ba})} + r_{\text{O}})$ (see Appendix A), is, respectively, 114pm, 132pm and 149pm [25].

3.2 Coordination number and bond lengths

A simple but yet effective way of characterising the atomic arrangement of the ABO_3 perovskite structures that will be analysed throughout this work is the computation of the lengths of the bonds which arise between each cation (i.e A and B) and each anion (i.e O). These bond lengths, which are depicted in Table 3.2 for the bulk cubic structure of CaTiO_3 , SrTiO_3 and BaTiO_3 , will be crucial for understanding the ground state of the aforementioned perovskite-like structures due to the fact that, as it has been already pinpointed, those structures yielding a value of the Goldschmidt Tolerance Factor different than unity will undergo a structural phase transition by means of either AFD or FE distortions thus leading to a modification of the bond lengths and, in the case of AFD, to a modification of the coordination number (hereinafter referred to as CN) of the A cation.

System	CN of A	Bond length /Å	CN of B	Bond length /Å
CaTiO_3	12	2.703	6	1.911
SrTiO_3	12	2.739	6	1.937
BaTiO_3	12	2.791	6	1.974

Table 3.2: Coordination number and bond lengths of both A (i.e Ca, Sr or Ba) and B (i.e Ti) cations in the bulk cubic structure of CaTiO_3 , SrTiO_3 and BaTiO_3 .

If one keeps in mind the schematic representation of the ideal ABO_3 bulk cubic structure sketched in Figure 1.1 as well as the relations between the ionic radii and the lattice constant for a cubic closed-sphere packing arrangement derived in the Appendix A, it is straightforward to realise that the bond lengths of A and B cations could have also been calculated by substituting the cubic lattice parameters tabulated in Table 3.1 into the expressions $\frac{\sqrt{2}a}{2}$ and $\frac{a}{2}$ respectively.

3.3 Band structure

In order to obtain the electronic band structure of the three perovskite-like oxides in their bulk cubic crystalline configuration, the Kohn-Sham equation has been computed on a set of points located within the 1BZ. Specifically, the incursion along the 1BZ has been made through the following path: $\Gamma \rightarrow \text{X} \rightarrow \text{M} \rightarrow \text{R} \rightarrow \Gamma \rightarrow \text{M} \rightarrow \text{X} \rightarrow \text{R}$.

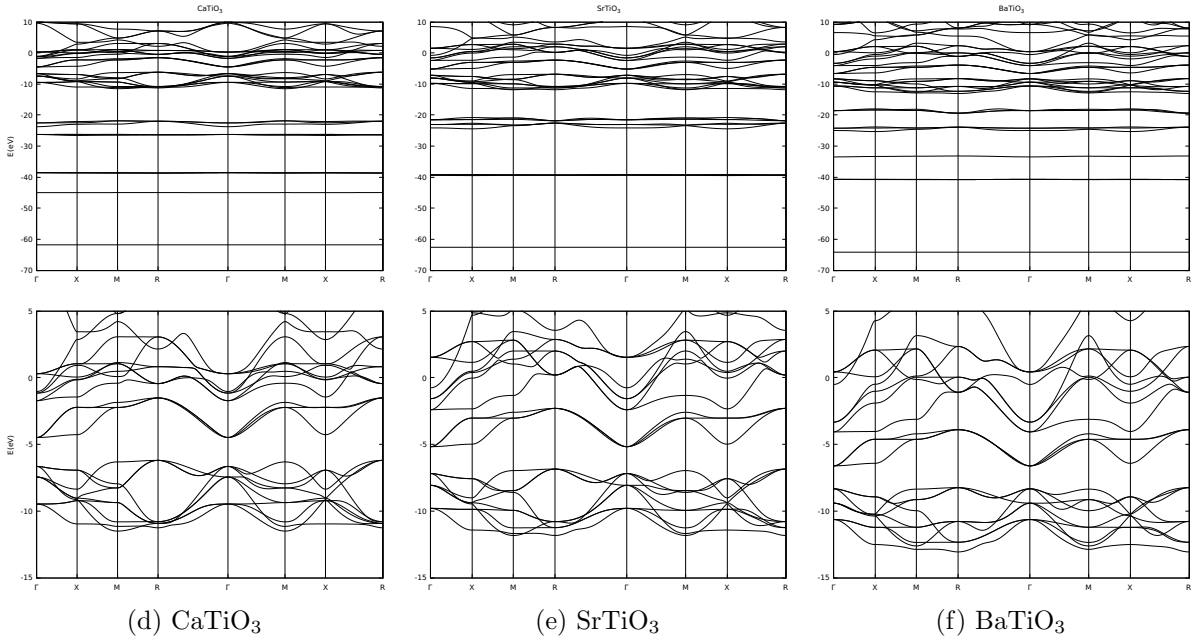


Figure 3.1: Full band structure (top row) and amplified band structure (bottom row) of CaTiO_3 ($E_F = -5.095\text{eV}$), SrTiO_3 ($E_F = -6.232\text{eV}$) and BaTiO_3 ($E_F = -7.709\text{eV}$) in their bulk cubic structure at the equilibrium lattice constant depicted in Table 3.1.

Bearing in mind that in a typical tight-binding textbook example the width of the electronic bands is related to the overlap between neighbouring atoms (i.e to the numerical value of $\langle \phi_v | \phi_u \rangle$) a quick inspection to the uppermost band structure displayed in Figure 3.1 shows the ionic character of these three materials as a set of well separated flat bands having, approximately, the same energy as the single orbitals giving rise to them is obtained. Nevertheless, specially if one analyses the bottommost band structure depicted in Figure 3.1, which zooms in on both the top of the valence band and the bottom of the conduction band of the three perovskite-like titanates, it is straightforward to realise that a covalent bonding nature is also displayed by these materials as the band structure at that level exhibits a significant dispersive character.

With the aim of performing a deeper analysis regarding the covalent character of the bonds arising in CaTiO_3 , SrTiO_3 and BaTiO_3 the projected density of states, hereinafter referred to as PDOS, which represents the number of electronic states with weight on an orbital μ available within a certain energy window, has been computed through the knowledge of the band structure of the aforementioned perovskite-like structures by means of the following expression:

$$g_\mu(E) = \frac{1}{N_{\vec{k}}} \sum_i^{\text{bands}} \sum_{\vec{k}} \sum_v C_{v_i}^*(\vec{k}) C_{\mu i}(\vec{k}) S_{v\mu}(\vec{k}) \delta(E - E_i(\vec{k})),$$

where $S_{v\mu}$ denotes the overlap matrix of the involved states, C_i represents the coefficient of the eigenvector $\Psi_i(\vec{K})$ and $N_{\vec{k}} = \frac{V}{a^3}^{\frac{1}{3}}$.

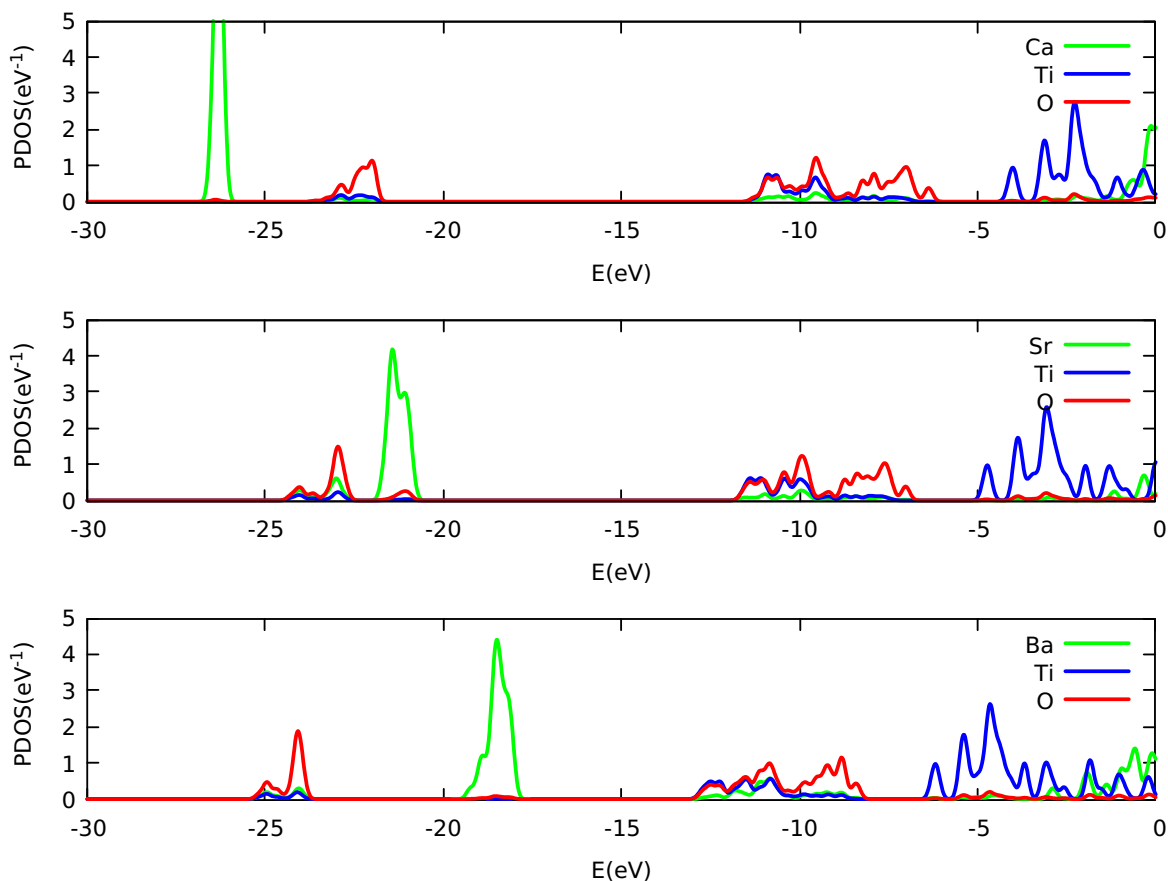


Figure 3.2: Projected density of states of CaTiO_3 , SrTiO_3 and BaTiO_3 in their bulk cubic structure at the equilibrium lattice constant depicted in Table 3.1 where the projections onto the A cation are shown in green, whereas the ones onto the Ti and O atoms are shown in blue and red respectively.

Following the same line of reasoning the so-called “fat bands”, which explicitly show the contribution of each atomic orbital to a certain band of the electronic band structure depicted in Figure 3.1, have also been computed yielding the electronic composition shown in Figure 3.3.

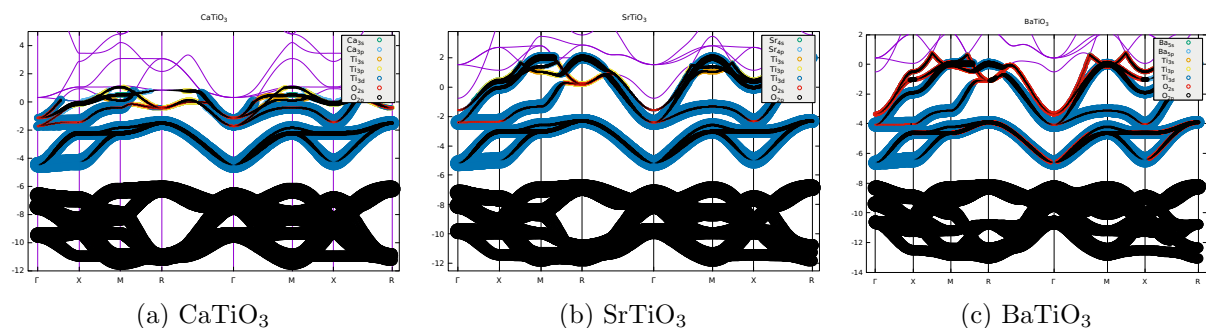


Figure 3.3: Electronic band structure of CaTiO_3 , SrTiO_3 and BaTiO_3 showing the contributions of O-2p and O-2s-like atoms (black and red respectively), Ti-3d, Ti-3p and Ti-3s-like atoms (dark blue, yellow and orange respectively) and p-like and s-like A atoms (light blue and green respectively).

When inspecting Figure 3.2 as well as Figure 3.3 one can certainly pinpoint the main common feature among these perovskite-like oxides: the top of the valence band has a predominant O- $2p$ character whereas the bottom of the conduction band is mainly composed of Ti- $3d$ -like atoms, specifically Ti- t_{2g} as the rupture of the degeneracy due to the electric field arising from the surrounding charge distribution of the oxygen atoms within the Ti chemical environment leads to a decrease in terms of energy of the d_{xy} , d_{xz} and d_{yz} orbitals which are collectively known as t_{2g} . Moreover, the both the “fat bands” and the PDOS clearly show a hybridization between the former orbitals enhancing therefore the covalent picture of these perovskite-like structures.

Despite the aforementioned similarities among these materials, one difference can be drawn when looking carefully to the PDOS depicted in Figure 3.2: the position of the peak corresponding to the A cation with respect to the O states moves towards higher energies as the number of electrons of the A cation increases, going from being lower in energy in CaTiO_3 to hybridize with the O atoms in SrTiO_3 to finally laying in higher energies in BaTiO_3 . It is worth noting that the same analysis can be made at the level of the “fat bands” represented in Figure 3.3 by carefully inspecting the differences concerning the O- $2s$ -like states, which are painted in red, between the three structures.

3.4 Born effective charges

Let k be a set of atoms submitted to a null macroscopic electric field. Under this constraint, the Born effective charge tensor Z^* is defined as the coefficient of proportionality relating the polarization per unit cell arising in the direction β and the atomic displacement of the set along the direction α [50]:

$$Z_{k,\alpha\beta}^* = \Omega_0 \left. \frac{\partial P_\beta}{\partial \tau_{k,\alpha}} \right|_{\mathcal{E}=0},$$

where, from a practical standpoint, the (α, β) elements of this tensor are computed as finite differences of the polarization with respect to small displacement of the corresponding atom along a given cartesian direction (i.e x , y and z).

$ATiO_3$	$Z_A^{*(T)}$	$Z_{Ti}^{*(T)}$	$Z_O^{*(T)}_{\parallel}$	$Z_O^{*(T)}_{\perp}$
Nominal	2	4	-2	-2
CaTiO_3	2.557	7.503	-5.912	-2.074
SrTiO_3	2.526	7.558	-5.950	-2.067
BaTiO_3	2.629	7.598	-5.988	-2.119

Table 3.3: Nominal and mean Born effective charge of each of the atoms located within the unit cell of CaTiO_3 , SrTiO_3 and BaTiO_3 . The subscripts \parallel / \perp denote the oxygen submitted to a displacement along the direction/perpendicular to the direction of the Ti-O bond.

It is worth remarking that, theoretically speaking, a diagonal symmetric tensor fulfilling the equation $\sum_k Z_{k,\alpha,\beta}^* = 0$ must be obtained for each ABO_3 perovskite-like structure as no net polarization should arise in a crystal as a result of its rigid displacement (i.e as the acoustic sum rule must be fulfilled).

Several conclusions can be drawn from the numerical values represented in Table 3.3.

Firstly, one can realize that for the three perovskite-like structures the Born effective charge of each atom highly differs from the nominal one (i.e from the one expected in a purely ionic material). In this former case the A atom, whose electronic configuration is given by $A : [xs^2]$, would transfer these two s electrons to oxygen atoms, whose electronic configuration is given by $O : [\text{He}]2s^22p^4$; and another electronic charge transfer would arise between the aforementioned oxygen atoms and the titanium, whose electronic configuration is given by $Ti : [\text{Ar}]3d^24s^2$, which would transfer these four electrons to the former.

Secondly, and directly linked with the first fact, one can easily realise that the Born effective charge of Ti and O is almost twice its nominal charge whereas for the rest of atoms the mismatch between both is not that significant. This feature can be explained in terms of the covalent bonding arising between the unoccupied d states of Ti and the non occupied p states of O, which has been already remarked when the band structure of the perovskite-like titanates was analysed, due to the fact that large values of $Z^{*(T)}$ have been found to have their origin in the rate of change of the overlap integrals concerning the so-called ‘‘off-site’’ hybridization under atomic displacements within the unit cell.

Finally, even though a band-by-band analysis should be carried out in order to clarify the underlying phenomena which give rise to the anomalous values of $Z^{*(T)}$ reported in Table 3.3, it seems reasonable to state that the A cation does not play a crucial role in the aforementioned hybridization as the Born effective charge values obtained for both titanium and oxygen atoms have been found to be extremely similar for CaTiO_3 , SrTiO_3 and BaTiO_3 (i.e the titanium atom is mainly affected by the octahedral chemical environment defined by the oxygen atoms). Furthermore, if one quickly inspects the Born effective charge values obtained for the aforementioned cation, it seems plausible too to affirm that the A-O bond displays a significant less covalent character which is in accordance with the fact that these atoms do not exhibit any occupied electronic state.

3.5 Maximally Localized Wannier Functions

Let the electronic state of a crystalline material be defined by a set of Bloch Functions, $\Psi_{n,\vec{k}}$, localized in the reciprocal space, which are ill-defined in the sense that the addition of a phase factor does not modify the electronic information carried by them, and let us consider a single isolated band n . Under these constraints, the aforementioned electronic representation can be expanded by a set of Wannier Functions, hereinafter referred to as WFs, localized in the reciprocal space, which, even though they are not eigenstates of the electronic Hamiltonian any more, they do expand the same Hilbert space as the set of equivalent Bloch Functions, and are related to the latter through the following Fourier-like transformation [51]:

$$|\vec{R}n\rangle = \frac{V}{(2\pi)^3} \int_{BZ} d\vec{k} e^{-i\vec{k}\cdot\vec{R}} |\Psi_{n,\vec{k}}\rangle.$$

If this approach is now generalised for a set of closed manifolds (i.e for set of distinct isolated groups of bands separated from each other by a significant energy gap) containing a certain number of bands (J), the unitary transformation between Bloch Functions and WFs adopts the following expression, where $U_{mn}^{(\vec{k})}$ represents a unitary matrix which arises as a result of the aforementioned non-uniqueness of the Bloch Functions [51]:

$$|\vec{R}n\rangle = \frac{V}{(2\pi)^3} \int_{BZ} d\vec{k} e^{-i\vec{k}\cdot\vec{R}} \sum_{m=1}^J U_{mn}^{(\vec{k})} |\Psi_{n,\vec{k}}\rangle.$$

In order to compute and plot the Wannier functions of SrTiO_3 , which will be of great utility when it comes to perform chemical bonding analysis, three well-separated manifolds, whose election has been based on the analysis of the band structure, have been used: one containing 9 bands (3 per oxygen) reflecting the O- $2p$ character of the top of the valence band (Manifold I), an other one containing 3 bands reflecting the Ti- t_{2g} character of the bottom of the conduction band (Manifold II) and, finally, one closed manifold mathematically constructed as the addition of the former two (Manifold III).

As it was stated above, generally speaking the WFs display a non-uniqueness character, so, in order to overcome this issue, the WFs of SrTiO_3 have been computed by means of the Maximally Localized approach [52] (i.e by iteratively minimising the sum over the set of different bands contained in each manifold of the quadratic spreads of the Wannier centers) yielding a set of J equivalent Maximally Localized Wannier Functions, hereinafter referred to as MLWFs, per unit cell for each closed manifold.

For the shake of completeness, some of the MLWFs as well as the quadratic spreads computed for SrTiO_3 are depicted below.

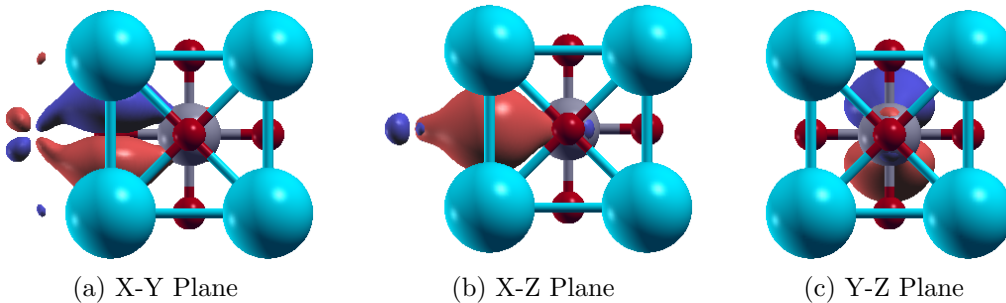


Figure 3.4: MLWF computed within the first manifold centred on a p_y oxygen atom displaying a π bond with a neighbouring d_{xy} -like Ti- t_{2g} atom.

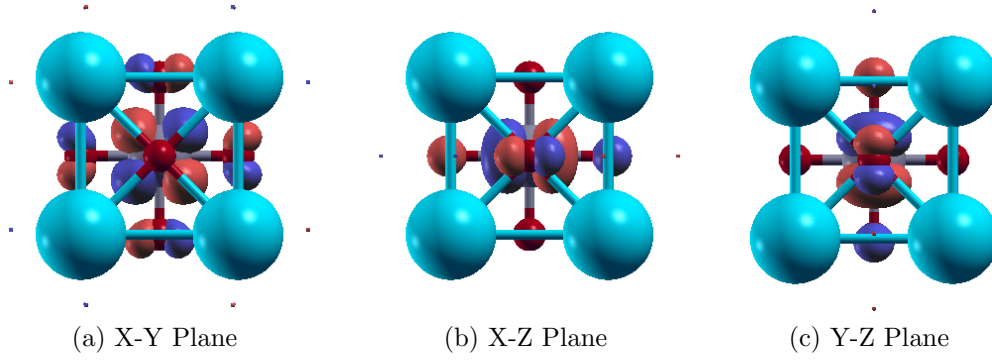


Figure 3.5: MLWF computed within the second manifold centred on a d_{xy} -Ti- t_{2g} atom displaying two π^* bonds with a neighbouring p_x -like O atom and a p_y -like one respectively.

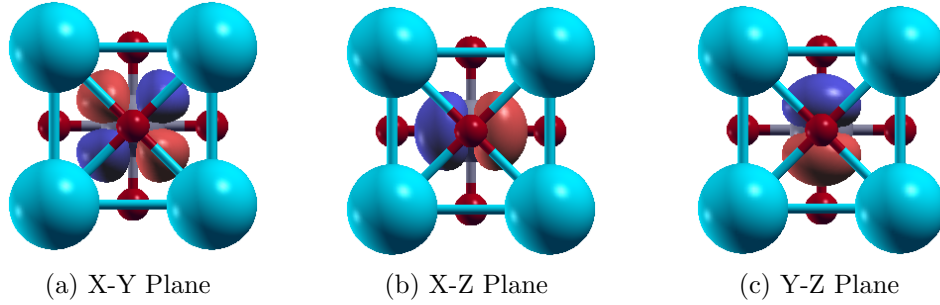


Figure 3.6: MLWF computed within the third manifold centred on a d_{xy} -Ti- t_{2g} showing an almost purely atomic character.

Manifold	Quadratic Spread / \AA^2
Manifold I	6×1.352 3×1.262
Manifold II	3×1.912
Manifold III	6×1.055 3×0.935 3×1.220

Table 3.4: Quadratic spreads of the Wannier Centres yielded by the MLWFs of each of the J bands embedded in each of the three distinct manifolds defined for the bulk cubic structure of SrTiO_3 .

Before deeply analysing several features regarding chemical bonding that can be directly drawn from the knowledge of the MLWFs, it is worth noting that these functions would be highly similar to the ones that one would obtain for CaTiO_3 and BaTiO_3 . This fact is not surprising at all as the similarity of the three perovskite-like crystals in terms of their electronic configuration has been already remarked not only when their band structure was analysed but also when $Z_{\text{Ti}}^{*(T)}$ and $Z_{\text{O}}^{*(T)}$ were found blind with respect to the A cation.

At the level of the previous results, even though the hybridization between the unoccupied d states of Ti and the $2p$ states of O was already known, the computation of the MLWFs gives rise to the knowledge of the type of bonding (e.g σ or π) through the degeneration of the spread of the Wannier Centres, hereinafter referred to as WCs, tabulated in Table 3.4. Specifically, within the second manifold all the bonds (d_{xy} with p_x and p_y , d_{yz} with p_z and p_y and d_{xz} with p_x and p_z) were found to be π^* -like; whereas within the one containing the 3 oxygen atoms of SrTiO_3 three bonds were found to be σ^* -like (p_x , p_y and p_z with dz^2) and the remaining 6 were found to be π -like (p_y with d_{xy} , p_z with d_{xz} , p_z with d_{yz} , p_x with d_{xy} , p_y with d_{yz} and p_x with d_{xz}).

Furthermore, it is worth noting that the manifold embedding both O- $2p$ and Ti- T_{2g} bands (i.e Manifold III) displays three distinct values for the spread of the WCs which was of course expected as this manifold has the intrinsic features of the former ones (i.e it exhibits π , π^* and σ^* bonds). Moreover, one can easily realise by inspecting Table 3.4 that the numerical values obtained for the quadratic spreads of the WCs of this manifold are significantly lower than those obtained for the unmixed manifolds as, in the former case, the MLWFCs were found to be more compact as a result of the increase of the electronic degrees of freedom.

Chapter 4

Ground state characterisation of CaTiO_3 , SrTiO_3 and BaTiO_3

The objective of this chapter is to analyse the structural and electronic properties that will arise in some of the low-symmetry phases of the three perovskite-like oxides (i.e in the ground states of CaTiO_3 and SrTiO_3 and in the ferroelectric tetragonal phase of BaTiO_3) studied herein by means of the so-called geometrical optimisation or structural relaxation.

4.1 Geometrical Optimization

It is well known that perovskite-like oxides display a wide range of energetically stable phases (i.e structural arrangements for which the free energy decreases) which can be identified by inspecting the local minima in the PES. In particular, when performing a multidimensional minimisation of the PES one can not only identify the equilibrium structures but also pinpoint the ground state, which corresponds to the global minimum, as well as the distorted structures connecting two low-symmetry phases, which appear within the PES analysis as saddle points.

In order to perform the aforementioned three dimensional optimization, the Conjugate Gradient Method [53], which can be regarded as an improved version of the Steepest Descent Algorithm [54] in terms of convergence, has been carried out within the framework of DFT. It is beyond the scope of this present work to fully depict the Conjugate Gradient Method; however, a brief description of the algorithm will be stated below for the sake of completeness:

1. An initial atomic arrangement is considered and the total energy is computed.
2. The gradient of the aforementioned energy, which depends explicitly on \vec{R} and \vec{r} within the framework of DFT, is computed by means of the Hellman-Feynman Theorem (see Appendix A) and the atoms are displaced along the direction defined by the negative value of the gradient (i.e along the direction of the forces).
3. A one dimensional minimisation procedure is carried out along the gradient line.

4. The minimum along the line is taken as the second trial atomic arrangement and the new forces arising from such configuration are computed.
5. The atoms are then displaced along the opposite direction of the new gradient which must be orthogonal to the first one.
6. The algorithm stops after n iterations, each of which is computed along a distinct orthogonal search direction, once the constraints specified in the FDF are fulfilled (i.e once the atomic forces and the elements of the stress tensor are less than a certain value, which would, ideally, be zero).

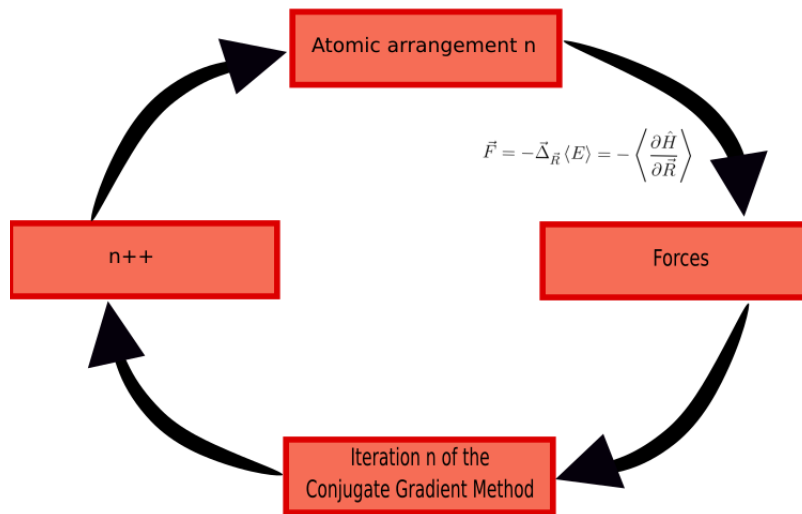


Figure 4.1: Schematic representation of the Conjugate Gradient's algorithm implemented throughout this present work so as to perform structural relaxation.

4.2 Structural Properties

Before going in depth in the analysis of the low-temperature phases of CaTiO_3 , SrTiO_3 and BaTiO_3 , it is worth noting that FE structural transitions do not imply a change in the number of formula units in the unit cell whereas in the case of AFD distortions such change takes place as otherwise it would be impossible to track any rotation because the periodically equivalent atoms would mirror the movement of the one contained in the unit cell thus leading to a net movement of the crystalline structure instead of to a rotation pattern.

The unit cells used to compute the magnitudes that will be analysed in this chapter, which are consistent with the colours used in Figure 1.1, are shown below.

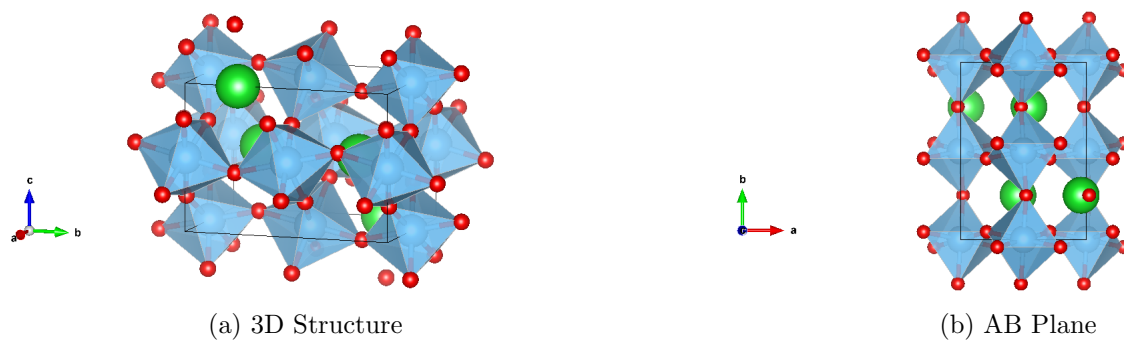


Figure 4.2: Orthorhombic unit cell of CaTiO_3 displaying an $a^-a^-c^+$ rotation pattern. Image obtained using VESTA [1].

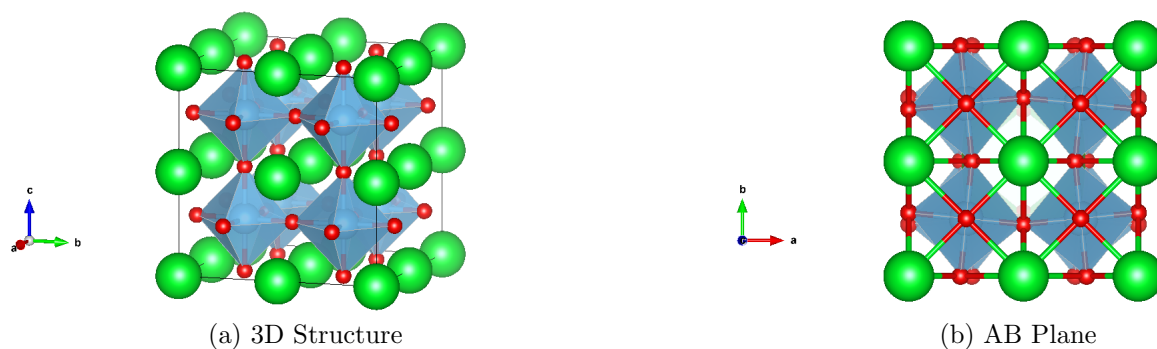


Figure 4.3: Tetragonal unit cell of SrTiO_3 displaying an $a^0a^0c^-$ rotation pattern. Image obtained using VESTA [1].

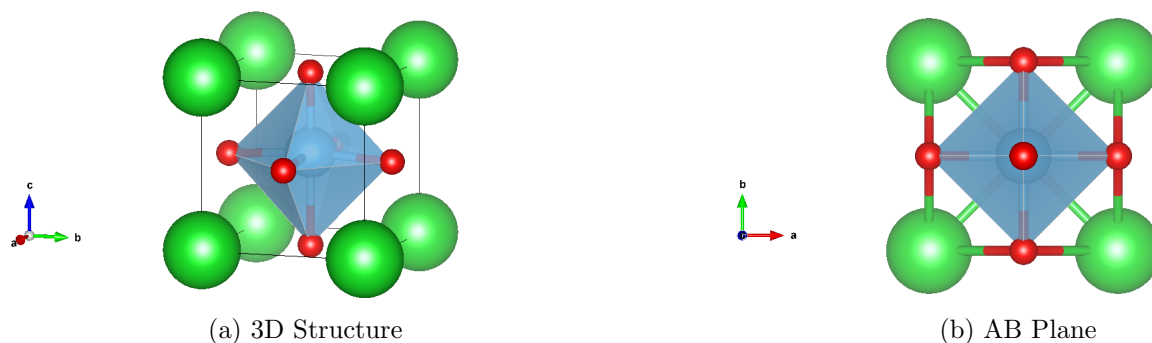


Figure 4.4: Schematic crystalline structure computed for BaTiO_3 in its bulk tetragonal phase displaying an atomic off-centering of Ti within the oxygen octahedra. Image obtained using VESTA [1].

By inspecting Figures 4.2, 4.3 and 4.4 it is effortless to distinguish between AFD and FE structural transitions in terms of the unit cell displayed by them. In particular, the unit cell of CaTiO_3 contains four formula units (i.e it is a supercell embedding twenty atoms) whereas that of SrTiO_3 contains eight formula units, although it would be sufficient to perform the simulations with a unit cell embedding just four formula unit. Likewise, because of the FE nature of the structural transition of bulk cubic BaTiO_3 towards its tetragonal phase, the unit cell displayed by it in its low-temperature phase coincides with that of the bulk cubic structure (i.e the unit cell contains just one formula unit).

4.2.1 Unit cell characterisation

With the objective of analysing the geometrical arrangement of the atoms within the low-symmetry phases of CaTiO_3 , SrTiO_3 and BaTiO_3 , which are depicted in Figures 4.2, 4.3 and 4.4 respectively, as well as their energetic stability, a detailed description of the lattice parameters and the energetic shift yielded by each crystalline structure, computed in the DFT Kohn-Sham framework (i.e being the energy of each geometrical phase given by Eq.(2.1.2)), once the structural relaxation was performed will be given below.

In particular, the energy shift has been computed through the following expression where LS denotes the low-symmetry phase considered while N indicates the amount of unit cells within that given supercell (i.e $N = 4$ for CaTiO_3 , $N = 8$ for SrTiO_3 and $N = 1$ for BaTiO_3):

$$\Delta E = \frac{1}{N}(E_{KS,LS} - N \times E_{KS,Cub}). \quad (4.1)$$

4.2.1.1 CaTiO_3

When carefully inspecting Tables 4.1 and 4.2 one can infer that the crystalline structure obtained for the ground state of CaTiO_3 by means of a DFT first-principles simulation is in accordance with the orthorhombic $a^-a^-c^+$ Glazer system reported by [55] and already depicted in Section 1.5. In particular, the theoretical lattice parameters computed, which differ from the experimental ones in less than 0.02\AA , are consistent with a perovskite-like structure embedded in the Pnma space group as $a \neq b \neq c$.

Numerical values	$a/\text{\AA}$	$b/\text{\AA}$	$c/\text{\AA}$	$\Delta E/\frac{\text{meV}}{\text{u.cell}}$
Theoretical	5.3999	7.5505	5.3066	-405.55
Theoretical (LDA functional) [55]	5.4122	7.5374	5.2898	

Table 4.1: Theoretical lattice parameters and energy shift with respect to the cubic phase reported for CaTiO_3 in its bulk orthorhombic structure.

Special importance must be attributed to the energy shift undergone by each formula unit of the orthorhombic unit cell which has been found to be significantly greater than the one yielded by both the ground state of SrTiO_3 and the tetragonal ferroelectric phase of BaTiO_3 which is tabulated in Tables 4.3 and 4.4 respectively. This striking reality, which is not as surprising for the tetragonal phase of BaTiO_3 as it is for the one displayed by SrTiO_3 owing to the fact that the former structure is not its ground state, as it was explained in Section 1.5, and, therefore, it does not constitute a global minimum of the PES, can be understood if one bears in mind the following regards:

- If one carefully inspects Table 1.1 it is clear that, even though SrTiO_3 exhibits an AFD instability too, its Goldschmidt Tolerance Factor differs from the one yielded by an ideal ABO_3 cubic structure by 0.009 whereas the difference calculated for CaTiO_3 is 0.027. As a result, and keeping in mind that the energy shift is directly related with the aforementioned Tolerance Factor, as it was reported by [6], it is reasonable to obtain highly distinct energy shifts for both types of perovskite-like ground states.

- Keeping in mind the correlation reported by [56] between higher energy shifts and higher temperature transitions from the ground state to the ideal bulk cubic structure, it is straightforward to foresee, when inspecting Section 1.5, that the energy shift of CaTiO_3 will be significantly greater than the one displayed by the ground state of SrTiO_3 .
- If one compares the bond lengths computed for CaTiO_3 in its bulk cubic structure (Table 3.2) with the ones obtained for the ground state of the aforementioned perovskite (Table 4.6) it is clear that the AFD-driven instability has strengthened the chemical bonds between A-O and B-O ions and, as a consequence, there has been an enhancement of the overlap between A/B and O orbitals, as it was explained in Section 1.3.1.2, which has ultimately led to an increase of the energetic stability of the crystalline structure.

Finally, for the sake of completeness, the Wyckoff positions [57] of each non-equivalent atom of the ground state of CaTiO_3 in its Pnma geometry have been depicted in Table 4.2.

Atom	Ca			Ti			O(1)			O(2)		
Coordinates	a	b	c	a	b	c	a	b	c	a	b	c
Theoretical	0.0432	1/4	0.9910	1/2	0	0	0.4798	1/4	0.0816	0.2922	0.0429	0.7069
LDA functional [55]	0.0480	1/4	0.9892	1/2	0	0	0.4776	1/4	0.0838	0.2927	0.0441	0.7063

Table 4.2: Theoretical atomic (fractional) coordinates of each chemical species of CaTiO_3 in its bulk orthorhombic structure.

It is worth remarking that the simulation performed under the framework of this bachelor thesis has been found to yield a set of Wyckoff positions differing in less than 0.005 fractional units from the ones reported by [55]. As a consequence, being both simulations performed by means of the same functional (Eq.(2.4)), the knowledge of the Wyckoff positions reported by [55] could be used as a reference for carrying out a series of tests with distinct pseudopotentials, sampling grids or basis functions among others approximations described in Section 2.

4.2.1.2 SrTiO_3

The structural and energetic parameters of the ground state of SrTiO_3 (i.e of the $a^0a^0c^-$ system), which reflect the I4/mcm space group nature of the aforementioned low-symmetry phase, already reported in Section 1.5, due to the fact that the tetragonality has been found to differ from unity, are depicted in Table 4.3.

Numerical values	$a/\text{\AA}$	$c/\text{\AA}$	c/a	$\delta/\text{f.u}$	$\alpha/^\circ$	$\Delta E/\frac{\text{meV}}{\text{u.cell}}$
Theoretical	3.85967	3.89359	1.00879	0.02505617	2.87	-6.28
Experimental	3.894	3.898	1.0005		2.1	

Table 4.3: Theoretical and experimental [34] lattice parameters, tetragonality, oxygen displacements (in fractional units), octahedral rotation angle and energy shift with respect to the cubic phase reported for SrTiO_3 in its bulk tetragonal structure .

Several aspects of the magnitudes tabulated above are worth discussing:

Firstly, it is worth mentioning that the crystalline structure has undergone a symmetry transition from a bulk cubic structure to a bulk tetragonal structure being both theoretical and experimental data regarding the lattice parameters displayed by the ground state of SrTiO_3 in perfect agreement; indeed, they differ in less than 0.04\AA . Moreover, it is worth noting that this structural change could have been predicted by means of the rotation angle tabulated in Table 4.3 as it was reported by [11] that, for a given perovskite-like structure displaying an AFD instability consisting in either in-phase or anti-phase rotations around the c axis, the BO_6 octahedra will be axially modified unless the trigonometric relation $\frac{a}{c} = \sqrt{2} \cos \phi$ holds, which is clearly not the case for the ground state analysed herein.

Secondly, when inspecting the oxygen displacements reported for the TiO_2 plane, it is straightforward to realise, and it could have been already pinpointed by looking at Figures 4.3 and 4.2, that the AFD distortion undergone by SrTiO_3 displays a smaller amplitude than the one undergone by CaTiO_3 which leads to greater atomic displacements that can be inferred from the Wyckoff positions depicted in Table 4.2. Once again this fact is not surprising as a decrease of the AFD distortion amplitudes for increasing Goldschmidt Tolerance Factors was already foreseen by [6].

Thirdly, the rotation angle calculated through the expression $\alpha = \arctan\left(\frac{\delta}{2 \times \frac{L}{2}}\right)$, where $L=0.5$ denotes the length of each formula unit embedded in the supercell, has been found to be consistent with the competitive nature of AFD and FE instabilities (i.e has been found to be lower than 5° [30]).

Finally, it is worth noting that the energy shift reported in Table 4.3 is slightly lower than the one yielded by the tetragonal ferroelectric phase of BaTiO_3 which is depicted in Table 4.4. Once again this fact is not surprising as it has been already remarked, when shedding light to the results obtained for the ground state of CaTiO_3 , that there is a correlation between the critical temperature at which the transition towards the bulk cubic crystalline structure takes place and the energy shift. Therefore, if one carefully inspects Section 1.5, the energy difference between these two perovskite-like titanates becomes obvious.

4.2.1.3 BaTiO_3

The structural and energetic data which will be used to characterise the unit cell of BaTiO_3 in its low-temperature tetragonal phase is depicted in Table 4.4.

Numerical values	$a/\text{\AA}$	$c/\text{\AA}$	c/a	$V/\text{\AA}^3$	$\Delta_{T-\text{Ti}}/\text{f.u}$	$\Delta_{T-\text{O1}}/\text{f.u}$	$\Delta_{T-\text{O2}}/\text{f.u}$	$\Delta E/\frac{\text{meV}}{\text{u.cell}}$
Theoretical	3.938139	3.999005	1.015455	62.023	0.015485	-0.021637	-0.015074	-10.3
Experimental	3.986	4.026	1.010	63.97	0.015	-0.023	-0.014	

Table 4.4: Theoretical and experimental [58] lattice parameters, tetragonality, volume of the unit cell, titanium and oxygen displacements (in fractional units) and energy shift with respect to the cubic phase reported for BaTiO_3 in its bulk tetragonal structure .

When inspecting the tetragonality factor reported in Table 4.4, it is clear that the aforementioned perovskite-like structure has undergone a greater distortion, in terms of axial elongation, than the ground state of SrTiO_3 which also displays a tetragonal structure and yields a value of 1.00879 for the tetragonality factor. However, if one bears in mind the Goldschmidt Tolerance Factors depicted in Table 1.1, it is straightforward to foresee the aforesaid difference as the Tolerance Factor of SrTiO_3 lies closer to unity than the one displayed by BaTiO_3 and, therefore, the former structure will be submitted to less significant distortions which will ultimately reaccommodate the cations within the unit cell.

In addition, it is worth mentioning that the atomic displacements, calculated with respect to the atomic position of the cation Ba, undergone by BaTiO_3 as a result of its phase transition are in full agreement with the Γ_{4-} soft mode-driven transition. In particular, the Ti cation has been displaced upwards whereas the oxygen O(1) (i.e the one located in the TiO_2 plane, specifically at $[1/2, 0, 1/2]$ in the bulk cubic structure) and the oxygen O(2) (i.e the one located in the BaO plane, specifically at $[1/2, 1/2, 0]$ in the bulk cubic structure) have undergone a downward displacement which, as one would expect when inspecting Figure 4.4, has been found to be greater for O(1).

In order to put an end to the analysis of the low-temperature tetragonal phase of BaTiO_3 it is almost mandatory to compute the macroscopic polarization arising in the direction defined by the c axis of this crystalline structure which will be tabulated below. Before doing so, it is worth explaining its origin: because of the above mentioned Ti and O displacements, and bearing in mind the admixture between ionic and covalent bonding that takes place among ABO_3 perovskites, which has already been pinpointed in the previous chapter, the longitudinal Ti-O bond length has been shortened and, therefore, the transfer of charge in this covalent framework has been encouraged (i.e the Born effective charges of both Ti and O atoms participating in the Ti-O π bonding significantly differ from the nominal ones and are also greater than the ones yielded by the same atoms in the bulk cubic structure). As a result of the aforesaid transfer of charges, the Coulomb interactions are great enough to counteract the short-range forces, thus leading to an FE instability.

$P_{z,the}/\mu\text{C} \times \text{cm}^{-2}$	$P_{z,exp}/\mu\text{C} \times \text{cm}^{-2}$
30.39	26.3

Table 4.5: Theoretical (th) and experimental (exp) [59] macroscopic polarization obtained for BaTiO_3 in its bulk tetragonal low-symmetry phase.

4.2.2 Band structure

With the aim of analysing the electronic structure of the ground state of CaTiO_3 and SrTiO_3 as well as that of the tetragonal low-temperature phase of BaTiO_3 the Projected Density of States has been computed for each perovskite-like structure being each non-equivalent atomic contribution plotted in Figure 4.5.

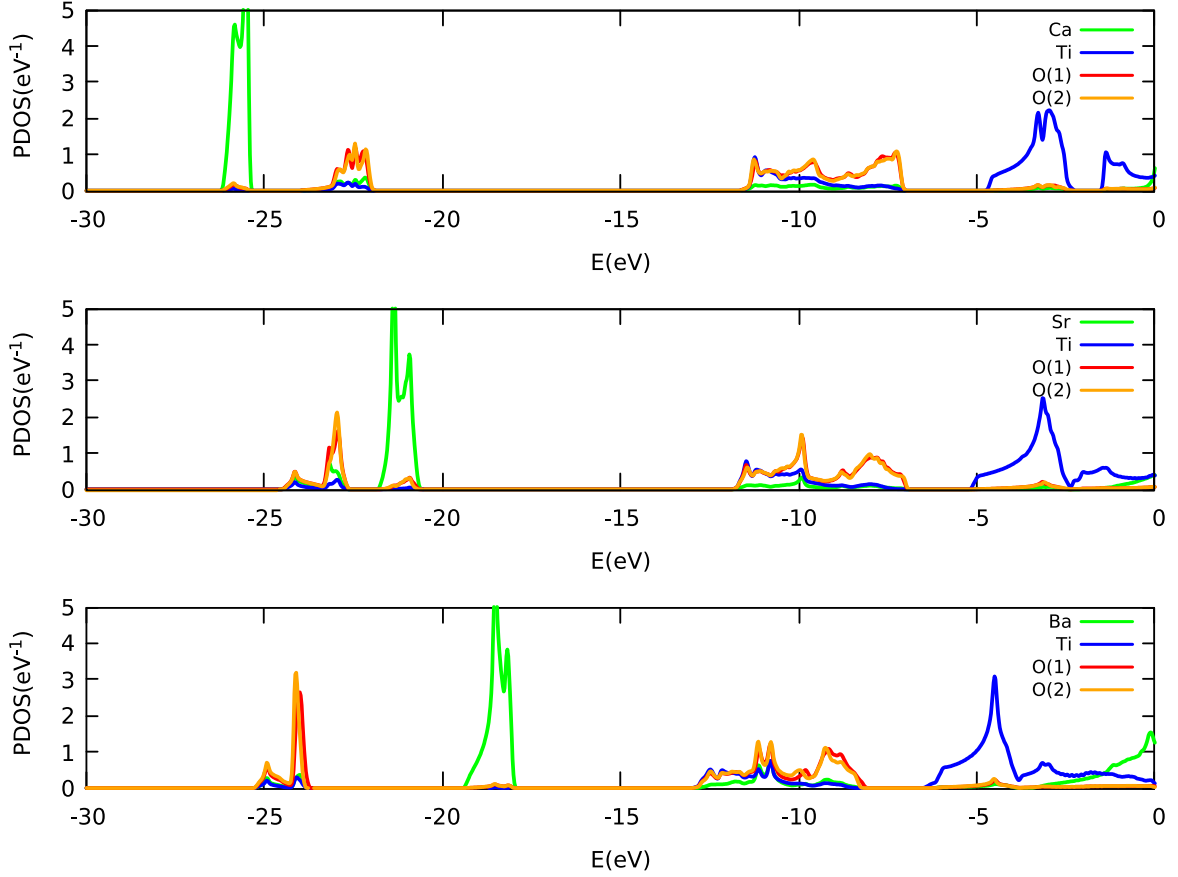


Figure 4.5: Projected density of states of CaTiO_3 , SrTiO_3 and BaTiO_3 in their bulk orthorhombic and tetragonal structure respectively at the equilibrium lattice constant depicted in Tables 4.1, 4.3 and 4.4 where the projections onto the A cation are shown in green, whereas the ones onto the Ti and the two non-equivalent O atoms are shown in blue, red and orange respectively.

At this point, and bearing in mind that bond lengths play an important role regarding orbital overlap, it is worth remarking both the similarities and differences between the PDOS computed for the ideal bulk cubic structure of the aforementioned perovskite-like crystals (Figure 3.2) and the PDOS depicted herein (Figure 4.5).

On the one hand, when inspecting the width of the peaks displayed by each atomic contribution it is straightforward, and barely unexpected as it has been already discussed in 1.3.1.2 as well as during the analysis of the PDOS computed for the cubic structure of the aforementioned perovskites, to realise that the bonds arising in such structures (i.e. in the low-symmetry phases of CaTiO_3 , SrTiO_3 and BaTiO_3) can be described in terms of an admixture of ionic and covalent bonding. Furthermore, the PDOS depicted above not only shows the same contributions around the energy gap as the PDOS computed for the ideal cubic structure (i.e. a predominant O-2p character in the uppermost region of the valence band and a predominant Ti-3d character in the bottommost region of the conduction band) but also the same behaviour of the position of the A-p peak with respect to the O-2s one.

On the other hand, if one carefully inspects the conduction band of both PDOS (Figures 3.2 and 4.5), it is clear that whereas in the cubic structure there is a "resonant" contribution arising from both Ti- t_{2g} and Ti- e_g states, that does not seem to be the case for the lower-symmetry phases in which the contribution arising from the Ti atom displays a

smoother behaviour. This fact can be understood within the Crystal Field Theory framework owing to the fact that a phase transition from cubic to tetragonal/orthorhombic symmetry implies a decrease regarding the symmetry of the Ti-3d complex from O_h to D_{4h}/D_{2h} respectively, thus modifying the number of unlike energy levels of d-orbitals from 2 in the bulk cubic structure to 4/5 in the tetragonal/orthorhombic crystalline structure (see Appendix A for further information). As a result of such degeneracy rupture, the possibility of finding an electron at a certain energy will increase as the degrees of freedom linked to the energetic position of d-orbitals have increased too and, therefore, the contribution arising from the Ti states will become smoother even though an orbital-by-orbital decomposition would result in a “resonant” behaviour.

Finally, it is worth remarking the different intensity of the contributions arising from the O-2s states between the bulk cubic structure of BaTiO_3 and its ferroelectric tetragonal structure. This can be easily understood if one realises that the off-centering movement of Ti towards the oxygen located at $[1/2, 1/2, 0]$ depicted in Figure 4.4 leads to a decrease in that given Ti-O bond length, thus increasing the overlap between both orbitals.

4.2.3 Coordination number and bond lengths

With the aim of fully characterise the geometry displayed by the low-symmetry phases of CaTiO_3 , SrTiO_3 and BaTiO_3 as well as to perform a deep analysis of the bonds that have been either reinforced or weakened as a result of a phase transition driven by the need to reaccommodate the undersized B or oversized A cations within the perovskite crystalline structure, the bond lengths of each cation have been computed.

4.2.3.1 CaTiO_3

The bulk cubic structure of CaTiO_3 yields a tolerance factor slightly greater than unity and, therefore, its phase transition, which is linked to the simultaneous condensation of the soft modes located at R and M , is driven by an AFD instability consisting in two identical anti-phase rotation patterns along the axes a and b and an in-phase rotation pattern along the c axis (i.e the $a^-a^-c^+$ Glazer system). The bond lengths displayed by both Ca and Ti cations in the ground state of CaTiO_3 sketched in Figure 4.2 are depicted in Table 4.6.

Atom(V) / Neighbouring atom(s)(H)	Ca / Å	Ti / Å	O / Å
Ca			1×2.294
			2×2.321
			1×2.406
		2×3.106	2×2.555
			2×2.645
			1×2.306
			1×3.081
Ti			2×1.940
	2×3.106		2×1.945
			2×1.950

Table 4.6: Neighbouring atoms and bond lengths (second, third and fourth column) of both Ca and Ti (second and third row) in the orthorhombic phase of CaTiO_3 .

At first glance, specially if one compares the data tabulated above with the one yielded by the ground state of SrTiO_3 and depicted in Table 4.7, it is straightforward to realise that the ground state of the former perovskite displays a higher degree of distortion than the former even though both present an AFD distorted phase. As a consequence, not only the energy gain is the greatest among the perovskites studied herein but also the coordination number and the bond lengths displayed by both cations are the ones that have been modified the most, as it can be pinpointed by looking at Figure 4.3, once the phase transition has taken place.

Regarding the bonds, it is worth remarking that in the ground state of CaTiO_3 the Ca cation does no longer present a 12-fold oxygen coordination but a 10-fold one in which nine of the oxygens are significantly closer to the aforesaid cation than in the bulk cubic structure (see Table 3.2) being the tenth oxygen located at a distance long enough (3.081\AA) to cease to be even considered part of the coordination polyhedron. Moreover, as a result of the geometry displayed by the ground state (i.e as a result of the different lengths of the orthorhombic lattice parameters a , b and c), the oxygens surrounding the central Ti of each unit cell within the supercell are located at different distances from it being all of them longer than in the bulk cubic structure.

4.2.3.2 SrTiO_3

The bulk cubic structure of SrTiO_3 yields a tolerance factor slightly greater than unity and, therefore, its phase transition is driven by a small tilting of the octahedra along the c axis, in particular by a R_{5-} soft mode. The bond lengths displayed by both Sr and Ti cations in the $a^0a^0c^-$ ground state sketched in Figure 4.3 are depicted in Table 4.7.

Atom(V) / Neighbouring atom(s)(H)	Sr / \AA	Ti / \AA	O / \AA
Sr			4×2.609
			4×2.729
			4×2.881
Ti			4×1.940
			2×1.947

Table 4.7: Neighbouring atoms and bond lengths (second, third and fourth column) of both Sr and Ti (second and third row) in the tetragonal phase of SrTiO_3 .

On the one hand, regarding the chemical bonds displayed by Ti, neither the coordination number of Ti nor the O-Ti-O bond angles differ from those tabulated in Table 3.2 for the bulk cubic structure of SrTiO_3 ; as a matter of fact, the only difference between the ground state and the cubic structure is the lengthening of the bonds of the O atoms located at $c = 1$ and $c = 0$ which is driven by the geometrical transition from a cubic structure to a tetragonal one by means of the elongation of the c axis.

On the other hand, regarding the chemical bonds displayed by Sr, it is straightforward to realise that the tilting of the octahedra along the c axis has led to the splitting of the 12 equivalent bond distances (2.739\AA) between Sr and O displayed by the cubic structure into four short, four medium and four long Sr-O distances. The medium distances correspond to the oxygens located at $c = 0$ in the Ti-centred scheme (i.e at $c = 1/2$ in the Sr-centred scheme), whereas the short distances are those related to two oxygens located

at $[1/2, 0, 1/2]$ in the Ti-centred scheme and at $c = 0.75$ in the supercell sketched in Figure 4.3 and to two oxygens located at $[0, 1/2, 1/2]$ in the Ti-centred scheme and at $c = 0.25$ in the Sr-centred supercell. Finally, the longest distances are those corresponding to the interchanged positions of the former (i.e two oxygens located at $[1/2, 0, 1/2]$ in the Ti-centred scheme and at $c = 0.25$ in the supercell sketched in Figure 4.3 and to two oxygens located at $[0, 1/2, 1/2]$ in the Ti-centred scheme and at $c = 0.75$ in the Sr-centred supercell).

4.2.3.3 BaTiO_3

The bulk cubic structure of BaTiO_3 yields a tolerance factor greater than unity and, therefore, its phase transition is driven by an off-centering displacement of Ti, in particular by a Γ_{4-} soft mode. The bond lengths displayed by both Ba and Ti cations in the ferroelectric tetragonal low-symmetry phase sketched in Figure 4.4 are depicted in Table 4.8.

Atom(V) / Neighbouring atom(s)(H)	Ba / Å	Ti / Å	O / Å
Ba			4×2.764
			4×2.786
			4×2.850
Ti			1×1.851
			1×2.148
			4×1.973

Table 4.8: Neighbouring atoms and bond lengths (second, third and fourth column) of both Ba and Ti (second and third row) in the tetragonal phase of BaTiO_3 .

If one inspects the chemical environment of Ti, it is straightforward to realise that the coordination number has not changed with respect to the bulk cubic structure as it was already predicted in Section 1.3.1.2. In particular, the oxygen atoms located in the $c = 1/2$ plane are no longer linked to the central Ti by a linear chain (i.e through an angle of 180°) as it can be seen in Figure 4.4; however, they do remain at the same distance of Ti (i.e 1.973Å) as the one yielded by the bulk cubic arrangement and depicted in Table 3.2. Moreover, the aforementioned movement of the Ti atom towards the oxygen located in the $c = 1$ plane leads to the shortening and lengthening of the two respective bonds parallel to the direction of displacement of the central Ti cation.

Likewise, if one keeps in mind the A-centred schematic representation of an ABO_3 perovskite, the atomic movements explained above will lead to the establishment of 4 short (those displayed by the oxygens located in the plane defined by $c = 1/2$ in the Ti-centred scheme and in the plane defined by $c = 1$ in the Ba-centred scheme), 4 medium (those displayed by the oxygens located in the plane defined by $c = 1$ and $c = 0$ in the Ti-centred scheme and in the plane defined by $c = 1/2$ in the Ba-centred scheme) and 4 long bond lengths (those displayed by the oxygens located in the plane defined by $c = 1/2$ in the Ti-centred scheme and in the plane defined by $c = 0$ in the Ba-centred scheme) between the Ba cation and the surrounding O atoms.

Chapter 5

Final considerations

This chapter aims at highlighting the main results obtained for the three perovskite-like crystalline structures analysed in their bulk cubic structure (Chapter 3) and in their low-symmetry phase (Chapter 4) through the first-principles code SIESTA. Moreover, a few words will be said about the improvements that could have been made at the level of the simulations. Finally, a brief discussion about the additional calculations and simulations that could have been carried out so as to provide the reader with a better overall picture of the nature of CaTiO_3 , SrTiO_3 and BaTiO_3 will be outlined and some future lines of research will be suggested.

5.1 Conclusions

First of all, it is worth remarking the power of DFT first-principles simulations as, even by performing the calculations within the framework of LDA, the results obtained for the three perovskite-like titanates depicted in Chapters 3 and 4 (e.g the lattice parameters of the bulk cubic structure of CaTiO_3 , SrTiO_3 and BaTiO_3 tabulated in Table 3.1 or the energy shifts and lattice parameters of the low-symmetry phases of the aforementioned perovskite-like oxides tabulated in Tables 4.1, 4.3 and 4.4, among others) have been found to be in full agreement with the experimental values reported by the authors cited therein.

Secondly, and in regards to the results obtained for the bulk cubic structure of the aforesaid perovskite-like titanates, it is worth mentioning that the computation of the band structure, specifically the width of the bands obtained; the so-called “fat bands”; the PDOS and the Born effective charges, specifically the huge difference reported therein between the nominal charges and the ones obtained for Ti and O \perp , has led to the main conclusion drawn in Chapter 3: the nature of the bondings arising in ATiO_3 crystalline structures can be regarded as an admixture of covalent and ionic character. In addition, it is worth noting that the computation of the “fat bands”, which are depicted in Figure 3.3, has shed light to the contribution of each orbital to both the conduction and the valence bands; in particular, it has been proven that the top of the valence band has a predominant O-2*p* character whereas the bottom of the conduction band displays a Ti-*t*_{2*g*} nature. Besides, the main difference between CaTiO_3 , SrTiO_3 and BaTiO_3 regarding their electronic properties has been pinpointed through the computation of the PDOS: the energetic range contribution of the A cation to the band structure of each of the perovskite-like titanates analysed throughout this thesis is correlated with the atomic number of the aforesaid cation; specifically, it has been shown that the hybridization between the orbitals of such cation and the O-2*s* states only takes place in SrTiO_3 , being

the A peak too low and too high in terms of energy to hybridize with the O-2s states of CaTiO₃ and BaTiO₃ respectively.

Thirdly, and in regards to the results obtained for the low-symmetry phases of CaTiO₃, SrTiO₃ and BaTiO₃ reported in Chapter 4, it is worth noting that the simulations performed therein have verified the predictions regarding the phase transitions sketched in Section 1.5 made based on the values of the Goldschmidt Tolerance Factors depicted in Table 1.1. In particular, the lattice parameters and atomic displacements reported in Tables 4.1, 4.2 and 4.3 for the ground states of CaTiO₃ and SrTiO₃ have proven to be in full agreement not only with the space group expected to be displayed by them (Pnma and I4/mcm respectively) but also with the characteristic AFD instability displayed by those structures yielding a value of t smaller than unity (i.e having an oversized A cation). In addition, the rotation angle computed for SrTiO₃ has proven to be consistent with the competitive nature of AFD and FE modes reported by [30]. Likewise, the results depicted in Table 4.4 have also succeeded in tracking both the upward and downward displacements undergone by Ti and O atoms respectively as well as the space group displayed by the distorted low-symmetry phase which ultimately leads to the FE mode predicted by means of the value of t yielded by the bulk cubic structure of BaTiO₃. Moreover, it is worth noting that all the energetic shifts reported in Tables 4.1, 4.3 and 4.4 are consistent with the correlation between the energy shift and the Goldschmidt Tolerance Factor reported by [6] as well as with the one found by [56] between the energy shift and the critical temperature at which the phase transition towards the high-symmetry crystalline structure takes place.

An other important feature to be highlighted in the framework of the low-symmetry phase analysis is the fact that the PDOS plotted in Figure 4.5 has proven to reflect both the Ti-O bond strengthening undergone by BaTiO₃, through the augmented intensity of the O-2s peak, and the O_h → D_{4h}/D_{2h} transition (see Appendix A) undergone by the Ti-3d complex, through the elimination of the highly energetic “resonances”. Finally, it should also be remarked that the bond lengths depicted in Tables 4.6, 4.7 and 4.8 are consistent with the space group displayed by each of the three perovskite-like oxides and its computation has proved the fact, which was stated in Section 1.3.1.1, that AFD instabilities do significantly distort the the coordination sphere of the A cation, which has been found to be specially true for the case of CaTiO₃ (Table 4.6), while leaving the coordination sphere of the Ti cation unperturbed.

5.2 Future work

5.2.1 Improvements

Even though, as it has been already remarked above, the results obtained through the simulations performed have been proven to be accurate, an undoubtedly improvement could have been made at the level of the approximations implemented in the code (see Chapter 2):

- An improved exchange-correlation energy functional, such as a hybrid one or that used under the framework of the Generalized Gradient Approximation (GGA), could have been used instead of working within the LDA framework. By doing so, even though the electronic charge density does not vary significantly in the perovskite-like structures belonging to the ATiO₃ family, the numerical values obtained would have

been more accurate as assuming that the value of $E_{xc}[n(\vec{r})]$ at an specific evaluation point depends only on the value yielded by the density at that point (i.e working within the LDA framework) might be regarded as a crude approximation.

Moreover, with the aim of completing the information reported in Chapters 3 and 4, the following simulations and/or calculations could have been performed:

- The MLWFs as well as the WCs could have been computed and plotted for the bulk cubic structure of CaTiO_3 and BaTiO_3 as well as for the low-symmetry phases of the three perovskite-like titanates studied throughout this bachelor thesis. Special importance should be given to the computation of the latter as it would shed light to the nature of the bondings (bonding or antibonding σ or π bonds) that have been weaken or strengthen as a result of the phase transition. In particular, one would expect to be able to pinpoint a significant change, with respect to the bulk cubic structure, regarding the π Ti-O longitudinal bonding of BaTiO_3 .
- The ground state of BaTiO_3 sketched in Figure 1.9 could have been simulated so as to have all the ground states of the three perovskite-like crystalline structures fully characterised. By doing so, one would expect to obtain a more significant energy shift as well as a polarization vector which does no longer point to the c axis as a result of the $R3m$ space group displayed by BaTiO_3 in its ground state.
- Born effective charges could have been computed for the three low-symmetry phases studied herein. This tensor, which would cease to be symmetric, would be a useful tool for tracking the structural arrangement changes reported in Chapter 4 by means of the analysis of the bond lengths.
- Lattice dynamics (i.e the study of atomic vibrations within the crystalline structure) could have been analysed in this bachelor thesis. In particular, phonon dispersion curves for the high-symmetry and low-symmetry phases of CaTiO_3 , SrTiO_3 and BaTiO_3 could have been computed with the ultimate goal of performing a deep analysis of both the instabilities arising therein and the competition among unstable modes within the soft mode approach.

5.2.2 Future lines of research

The results depicted herein for the high and low-symmetry phases of CaTiO_3 , SrTiO_3 and BaTiO_3 have opened the door to further lines of research focused on the deeper understanding of the phenomena analysed throughout this bachelor thesis:

- The study of the cooperation and/or competition arising among different soft modes (i.e those responsible for AFD and FE distortions) and hard modes (i.e those responsible for Jahn-Teller distortions and breathing modes), which have not been studied herein, by means of the couplings found when expanding the free energy of a given perovskite.
- The development of a vibronic coupling model able to accurately predict both the Glazer system and the rotation angles displayed by the ground states of CaTiO_3 and SrTiO_3 , among others ABO_3 perovskite-like oxides, without relying on steric arguments.
- The study of the dependence of the Gibbs free energy state function on T , P and other relevant parameters by means of a second-principles simulation.

Appendix A: Further physical concepts

In this section some of the concepts mentioned in the previous chapters will be developed for the sake of clarity even though they are not crucial for the comprehension of the work.

Derivation of Goldschmidt Tolerance Factor

Let us consider an ideal ABO_3 cubic perovskite (i.e a perovskite-like structure yielding a numerical value of $t=1$) and let us focus on the AO and the BO_2 plane, both of them sketched in Figure 1.

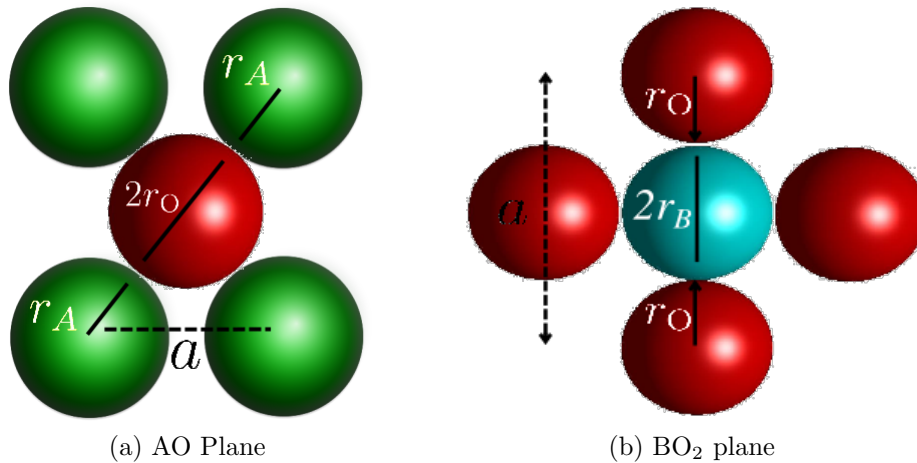


Figure 1: Schematic representation of an ideal ABO_3 cubic perovskite displaying a closed-sphere packing structure.

Under the constraint of closed-sphere packing the following relations between the cubic lattice parameter, a , and the ionic radii, r_i , hold:

$$\begin{aligned}
 \sqrt{2}a &= 2r_A + 2r_O \\
 \sqrt{2}(r_B + r_O) &= r_A + r_O \\
 1 &= \frac{r_A + r_O}{\sqrt{2}(r_B + r_O)} \\
 t &= \frac{r_A + r_O}{\sqrt{2}(r_B + r_O)},
 \end{aligned}$$

where the Pythagorean Theorem has been used in the first equality and the relation obtained from the analysis of the BO_2 plane (i.e $a = 2r_B + 2r_O$) has been used in the second one.

Hohenberg-Kohn Theorems

The two Hohenberg-Kohn theorems, which set the basis of DFT, will be stated below. They both can be verified easily and their proof can be consulted in [38].

Theorem I: For any system of interacting particles in an external potential $V_{ext}(\vec{r})$, the density is uniquely determined (i.e the external potential is a unique functional of the density)

Theorem II: A universal functional for the energy, $E[n]$, can be defined in terms of the density. The exact ground state is the global minimum value of this functional.

Kohn-Sham equations

In the framework of DFT the KS equation is the Schrödinger-like equation of a fictitious system of n non-interacting particles which yields the same electronic charge density as the original one made up of interacting particles.

$$\left[-\frac{1}{2}\nabla^2 + V_{eff}(\vec{r})\right]\phi_n(\vec{r}) = \epsilon_n\phi_n(\vec{r})$$

The electronic charge density of the aforementioned auxiliary system, which is needed in order to compute E_{el} , is calculated as it follows:

$$n(\vec{r}) = \sum_n^{occ} |\phi_n(\vec{r})|^2$$

Hellmann-Feynman Theorem

Let $|\Psi_\lambda\rangle$ be an eigenstate of the hamiltonian operator \hat{H}_λ associated with an eigenvalue E_λ . Under these constrains the following relations hold:

$$\begin{aligned} \frac{\partial E}{\partial \lambda} &= \left\langle \frac{\partial \Psi}{\partial \lambda} \left| \hat{H} \right| \Psi \right\rangle + \left\langle \Psi \left| \frac{\partial \hat{H}}{\partial \lambda} \right| \Psi \right\rangle + \left\langle \Psi \left| \hat{H} \right| \frac{\partial \Psi}{\partial \lambda} \right\rangle \\ &= E \left\langle \frac{\partial \Psi}{\partial \lambda} \left| \Psi \right\rangle + \left\langle \Psi \left| \frac{\partial \hat{H}}{\partial \lambda} \right| \Psi \right\rangle + E \left\langle \Psi \left| \frac{\partial \Psi}{\partial \lambda} \right\rangle \right. \\ &= E \frac{\partial}{\partial \lambda} \times \langle \Psi | \Psi \rangle + \left\langle \frac{\partial \hat{H}}{\partial \lambda} \right\rangle = \left\langle \frac{\partial \hat{H}}{\partial \lambda} \right\rangle, \end{aligned}$$

where the eigenvector equation (i.e $\hat{H}|\Psi\rangle = E|\Psi\rangle$) has been used in the second equality and the normalization condition (i.e $\langle \Psi | \Psi \rangle = 1$) has been applied to the third one.

Crystal Field Theory

It is well known that when solving the Schrödinger equation for a one-electron body the so-called atomic orbitals (s , p , d , f) naturally arise as they represent the eigenstate of the atomic Hamiltonian. These orbitals, in spite of their different spatial location, are degenerated (i.e their energy is the same) in an isolated atom/ion framework.

However, when the atom/ion is located within a given chemical environment, the electric field created by it lifts the degeneracy of the orbitals of the former atom/ion, thus leading to a set of energetically distinct orbitals.

In an ABO_3 perovskite-like oxide having a transition metal acting as a B cation the aforementioned rupture of the degeneracy, driven by the chemical environment defined by the TiO_6 octahedra, will take place among the d -orbitals sketched in Figure 2.

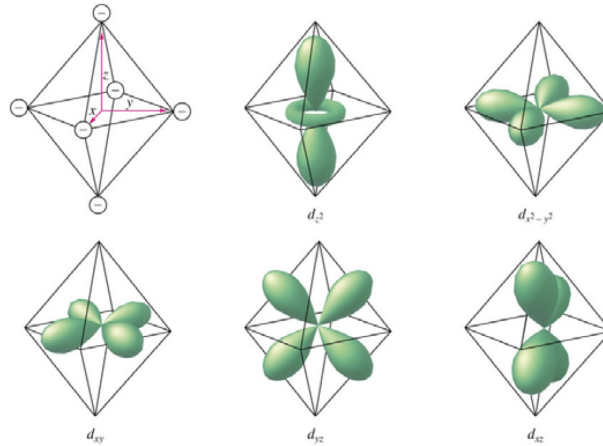


Figure 2: Schematic representation of the five ideally degenerated d -orbitals.

It is beyond the scope of this Appendix to provide a detailed description of such phenomenon, which can be found in [60]. Nevertheless, for the sake of comprehension, the orbital splitting, predicted by the Crystal Field Theory (hereinafter referred to as CFT), that will be undergone by the Ti cation in each of the ABO_3 structures that have been analysed throughout this thesis will be depicted below. Nonetheless, it is worth remarking that CFT is based on the following two assumptions and, therefore, it might lead to inaccurate predictions, specially if one bears in mind the mixed ionic-covalent character of the Ti-O bonds arising in the three perovskite-like structures analysed herein:

1. Both the metal and the ligands are treated as point charges.
2. Only electrostatic interactions between them are taken into account (i.e their bonding is considered to be purely ionic).

In particular, Figure 3 represents the d -orbital splitting taking place in the bulk cubic structure of $CaTiO_3$, $SrTiO_3$ and $BaTiO_3$ in which the TiO_6 chemical environment corresponds to the O_h point group (i.e an octahedral crystal field); Figure 4 represents the d -orbital splitting taking place in both the ground state of $SrTiO_3$ and in the ferroelectric tetragonal low-symmetry phase of $BaTiO_3$, in which the TiO_6 chemical environment corresponds to the D_{4h} point group (i.e an octahedral crystal field elongated along the cartesian direction defined by the c axis); and, finally, Figure 5 represents the d -orbital splitting taking place in the ground state of $CaTiO_3$ in which the chemical environment defined by TiO_6 has seen its symmetry lowered as a result of the orthorhombic crystalline structure of the given perovskite.

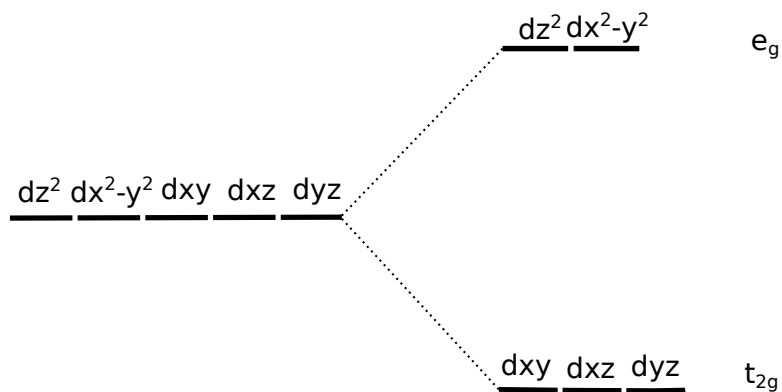


Figure 3: Crystal field splitting diagram for a transition metal in an O_h geometry fixed by the ligands.

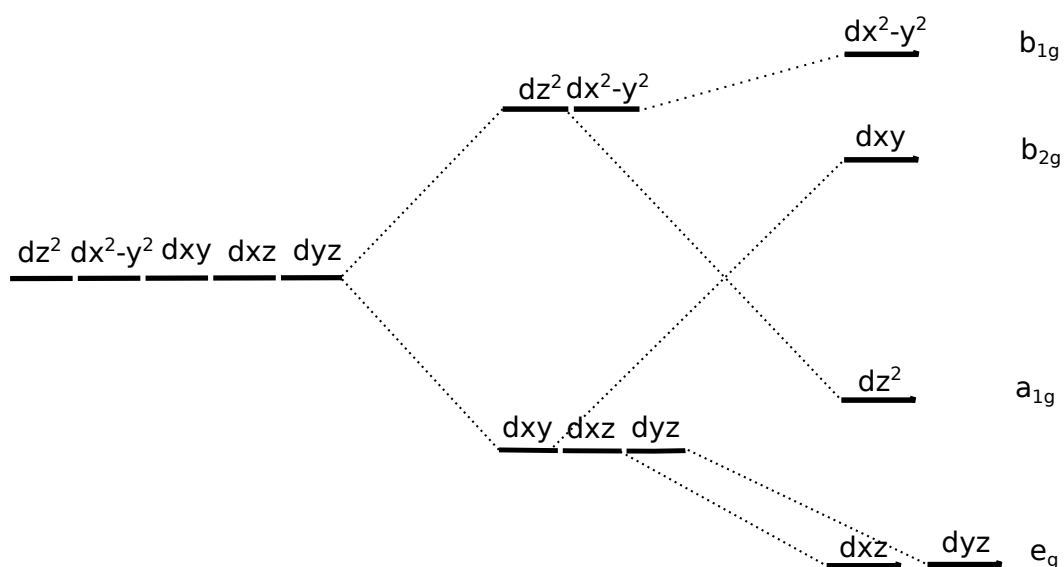


Figure 4: Crystal field splitting diagram for a transition metal in a D_{4h} geometry fixed by the ligands.

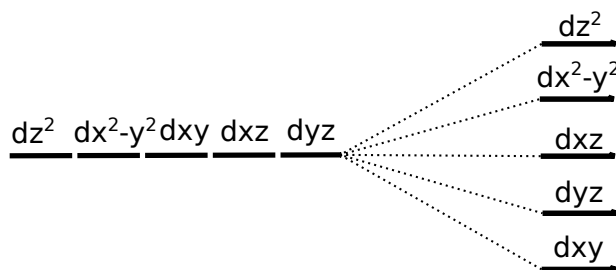


Figure 5: Crystal field splitting diagram for a transition metal in a D_{2h} fixed by the ligands.

Bibliography

- [1] K. MOMMA; F. IZUMI. 2011. VESTA 3 for three-dimensional visualization of crystal, volumetric and morphology data. *Journal of Applied Crystallography*, **44**(6), pp. 1272-1276.
- [2] E.A. LOMBARDO; M.A. ULLA. 1997. Perovskite oxides in catalysis; past, present and future. *Research on Chemical Intermediates*, **24**(5), pp. 581-592.
- [3] J. PÉREZ-RAMÍREZ; B. VIGELAND. 2005. Perovskite membranes in ammonia oxidation: towards process intensification in nitric acid and manufacture. *Angewandte Chemie*, **44**(7), pp. 1112-1115.
- [4] P. GHOZEZ; J. JUNQUERA. 2003. Critical thickness for ferroelectricity in perovskite ultrathin films. *Nature*, **422**(6931), pp. 596-509.
- [5] GLAZER.A.M. 1972. The Classification of Tilted Octahedra in Perovskites. *Acta Crystallographica Section B*, **28**, pp. 3384-3392.
- [6] CHEN.P [et al.]. 2018. Energetics of oxygen-octahedra rotations in perovskite oxides from first principles. *Physical Review B*, **97**(2), pp. 24113.
- [7] WOODWARD P.M. 1996. Octahedral Tilting in Perovskites. I. Geometrical Considerations. *Acta Crystallographica Section B*, **53**, pp. 32-43.
- [8] WINTER.M.J. 2016. *Chemical Bonding*. 2nd. ed. Oxford: Oxford Chemistry Primers. ISBN 0198700954.
- [9] GARCÍA-FERNÁNDEZ.P [et al.]. 2010. Key Role of Covalent Bonding in Octahedral Tilting in Perovskites. *The Journal Of Physical Chemistry Letters*, **1**(3), pp. 647-651.
- [10] CAMMARATA.A; RODINELLI.J.M. 2014. Covalent dependence of octahedral rotations in orthorhombic perovskite oxides. *The Journal of Chemical Physics*, **141**(11), pp. 114704.
- [11] HOWARD.C.J; STOKES.H.T. 1998. Group-Theoretical Analysis of Octahedral Tilting in Perovskites. *Acta Crystallographica Section B*, **54**, pp. 782-789.
- [12] WOODWARD P.M. 1996. Octahedral Tilting in Perovskites. II. Structure Stabilizing Forces. *Acta Crystallographica Section B*, **53**, pp. 44-46.
- [13] MARTIN.R.M. 2004. *Electronic Structure: Basic Theory and Practical Methods*. Cambridge: Cambridge University Press. ISBN 9780511805769.
- [14] VALASEK.J. 1924. Dielectric anomalies in rochelle salt crystals. *Physical Review Journals Archive*, **24**(5), pp. 560-568.

- [15] HAERTLING G.H. 2006. Ferroelectric ceramics: History and technology. *Journal of the American Ceramic Society*, **82**(4), pp. 797-818.
- [16] PAYNE.D.J [et al.]. 2006. Electronic Origins of Structural Distortion in Post-Transition Metal Oxides: Experimental and Theoretical Evidence for a Revision of the Lone Pair Model. *Physical Review Letters*, **96**(15), pp. 157403.
- [17] COCHRAN.W. 1960. Crystal Stability and the Theory of Ferroelectricity. *Advances in Physics*, **9**(36), pp. 387-423.
- [18] HARRISON.W.A. 1980. *Electronic Structure and the Properties of Solids*. New York: Dover Publications. ISBN 0486660214.
- [19] GHOSEZ.P; JUNQUERA.J. 2006. *Handbook of Theoretical and Computational Nanotechnology*. American Scientific Publishers. Chapter 13, pp.623-728. ISBN 1588830519.
- [20] DEVONSHIRE.A.F. 1949. XCVI. Theory of barium titanate. *The London, Edinburgh, and Dublin Philosophical Magazine and Journal of Science*, **40**(309), pp. 1040-1063.
- [21] ZHANG.Q. 2012. *Properties of Ferroelectric Perovskite Structures under Non-equilibrium Conditions* [online]. PONOMAREVA.I.(supervisor.). PHD Thesis University of South Florida. [Accessed: 18-12-2019]. Available at: USF.
- [22] LEMANOV.V [et al.]. 1999. Perovskite CaTiO_3 as an incipient ferroelectric. *Solid State Communications*, **110**(11), pp. 611-614.
- [23] SCHNEIDER.T; BECK.H; STOLL.E. 1975. Quantum effects in a n-component vector model for structural phase transitions. *Physical Review B*, **13**(3), pp. 1123-1130.
- [24] GOLDSCHMIDT.V.M. 1926. Die Gesetze der Krystallochemie. *Die Naturwissenschaften*, **21**(14), pp. 447-485.
- [25] R.D.SHANNON. 1976. Revised effective ionic radii and systematic studies of interatomic distances in halides and chalcogenides. *Acta Crystallographica Section A*, **32**(5), pp. 751-767.
- [26] VANDERBILT.D; SAI.N. 2000. First-principles study of ferroelectric and antiferrodistortive instabilities in tetragonal SrTiO_3 . *Physical Review B*, **62**(21), pp. 13942-13950.
- [27] KORNEV.A.I [et al.]. 2006. Phase Diagram of $\text{Pb}(\text{Zr,Ti})\text{O}_3$ Solid Solutions from First Principles. *Physical Review Letters*, **97**(15), pp. 157601.
- [28] BENEDECK.N.A; MULDER.A.T; FENNIE.C.J. 2012. Polar octahedral rotations: a path to new multifunctional materials. *Journal of Solid State Chemistry*, pp. 11-20.
- [29] BOUSQUET.E [et al.]. 2008. Improper ferroelectricity in perovskite oxide artificial superlattices. *Nature*, **452**(7188), pp. 732-736.
- [30] ÍÑIGUEZ.J [et al.]. 2018. Cooperative Couplings between Octahedral Rotations and Ferroelectricity in Perovskites and Related Materials. *Physical Review Letters*, **120**(19), pp. 197602.

- [31] BUSSMAN-HOLDER.A; BÜTTNER.H; BISHOP A.R. 2007. Polar-Soft-Mode-Driven Structural Phase Transition in SrTiO₃. *Physical Review Letters*, **99**(16), pp. 167603.
- [32] GHOSEZ.P [et al.]. 1999. Lattice dynamics of BaTiO₃, PbTiO₃, and PbZrO₃: A comparative first-principles study. *Physical Review B*, **60**(2), pp. 836-843.
- [33] A.ROUSHOWN; M.YASHIMA. 2008. Structural phase transition and octahedral tilting in the calcium titanate perovskite CaTiO₃. *Solid State Ionics*, **180**, pp. 120-126.
- [34] F.W.LYTLE. 1964. X-Ray Diffractometry of Low-Temperature Phase Transformation in Strontium Titanate. *Journal of Applied Physics*, **35**(7).
- [35] H.ZHANG. 2013. A theory for structural phase transitions in BaTiO₃ single crystal and PbZrO₃ – xPbTiO₃ solid solution. *AIP Advances*, **3**(4).
- [36] SOLER.J [et al.]. 2002. The SIESTA method for ab initio order-N materials simulation. *Journal of Physics: Condensed Matter*, **14**(11), pp. 2745-2779.
- [37] KHON.W; SHAM.L.J. 1965. Self-consistent equations including exchange and correlation effects. *Physical Review Journals Archive*, **140**(4A), pp. A1133-A1138.
- [38] HOHENBERG.P; KOHM.W. 1964. Inhomogeneous electron gas. *Physical Review Journals Archive*, **136**(3B), pp. B864-B871.
- [39] HAMAN.D.R; SCHLÜTER.M; CHIANG.C. 1979. Norm-Conserving Pseudopotentials. *Physical Review Letters*, **43**(20), pp. 1494-1497.
- [40] PHILLIPS.J.C; KLEINMAN.L. 1959. New Method for Calculating Wave Functions in Crystals and Molecules. *Physical Review Journals Archive*, **116**(2), pp. 287-294.
- [41] CHADI.D.J; COHEN.M.L. 1973. Special Points in the Brillouin Zone. *Physical Review B*, **8**(12), pp. 5747-5753.
- [42] GILAT.G; RAUBENHEIMER.L.J. 1966. Accurate Numerical Method for Calculating Frequency-Distribution Functions in Solids. *Physical Review Journals Archive*, **147**(2), pp. 670.
- [43] MONKHORST.H.J; PACK.J.D. 1976. Special points for the brillouin zone. *Physical Review B*, **13**(12), pp. 5188-5192.
- [44] ARTACHO.E [et al.]. 2001. Numerical atomic orbitals for linear-scaling calculations. *Physical Review B*, **64**(28), pp. 235111.
- [45] KENSEN.F. 2007. *Introduction to computational chemistry*. 2nd. ed. Odense: University of Southern Denmark. ISBN 139780470011867.
- [46] ARTACHO.E [et al.]. 2008. The SIESTA method; developments and applicability. *Journal of Physics: Condensed Matter*, **20**(6), pp. 064208.
- [47] F.D.MURNAGHAN. 1944. The compressibility of media under extreme pressures. *National Academy of Science of the United States of America*, **30**(9), pp.244-247.
- [48] K.M.RABE; P.GHOSEZ. 2007. *Modern ferroelectrics*. Topics of Applied Physics. Berlin: Springer. pp. 111-166. ISBN 9783540345909.

- [49] R.E.COHEN; W. ZHIGANG; D.J. SINGH. 2004. Comparing the weighted density approximation with the LDA and GGA for ground-state properties of ferroelectric perovskites. *Physical Review B*, **70**(10), pp. 104112.
- [50] M.BORN; M.GOPPERT-MAYER. 1993. *Dynamische Gittertheorie der Kristalle*. Handbuch der Physik.
- [51] G.H. WANNIER. 1937. The structure of electronic excitation levels in insulating crystals. *Physical Review Journals Archive*, **52**(3), pp. 191-197.
- [52] N.MAZARI; D.VANDERBILT. 1997. Maximally localized generalized Wannier functions for composite energy bands. *Physical Review B*, **56**(20), pp. 12847-12865.
- [53] M.R.HESTENES; E.STIEFEL. 1952. Methods of Conjugate Gradients for Solving Linear Systems. *Journal of Research of the National Bureau of Standards*, **49**(6).
- [54] A.CAUCHY. 1847. Méthode générale pour la résolution des systèmes d'équations simultanées. *Comptes Rendus de l'Académie des Sciences*, **10**(383), pp. 399-402.
- [55] E.COCKAYNE; B.P.BURTON. 2000. Phonons and Static Dielectric Constant in CaTiO_3 from First Principles. *Physical Review B*, **62**(6), pp. 3735-3743.
- [56] J.C.WODEL; J.ÍÑIGUEZ. 2004. Testing simple predictors for the temperature of a structural phase transition. *Physical Review B*, **90**(1), pp. 014105.
- [57] R.W.G. WYCKOFF. 1922. *The analytical expression of the results of the theory of space-groups*. 2nd. ed. Washington DC: Carnegie Institute of Washington.
- [58] SHIRANE.G; DANNER.H; REPINSKY.R. 1957. Neutron Diffraction Study of Orthorhombic BaTiO_3 . *Physical Review Journals Archive*, **105**(3), pp. 856-860.
- [59] H.H.WIEDER. 1955. Electrical Behavior of Barium Titanate Single Crystals at Low Temperatures. *Physical Review Journals Archive*, **99**(4), pp. 1161-1165.
- [60] L.E.ORGEL. 1960. *An introduction to transition-metal chemistry: Ligand-Field theory*. Methuen. ISBN 9780416634402.